Journal of Materials Research and Technology 40 (2026) 1364–1380

Contents lists available at ScienceDirect

Journal of Materials Research and Technology

journal homepage: www.elsevier.com/locate/jmrt

Microstructural evolution and high-temperature deformation behavior of wire arc additively manufactured Inconel 718 forging Preforms: Toward a hybrid Additive–Forging Process

Sambhaji Kusekar [a], Prashant Dhondapure [b], Mohammad Jahazi [b], Showmik Ahsan [c], Henry Young [c], Tushar Borkar [a,*]

[a] Department of Mechanical Engineering, Cleveland State University, OH, 44115, USA
[b] Department of Mechanical Engineering, École de Technologie Supérieure, Montreal, QC, H3C 1K3, Canada
[c] Department of Mechanical Engineering, Wright State University, OH, 45435, USA

ARTICLE INFO

Keywords:
Wire arc additive manufacturing (WAAM)
AM preform
Hybrid AM
Hot compression testing (HCT)
Dynamic recrystallization (DRX)
Dynamic recovery (DRV)
Inconel 718

ABSTRACT

Hybrid manufacturing routes combine additive manufacturing (AM) with conventional methods. They offer a potentially faster, more economical pathway to produce engineered components with performance that equals or exceeds that of wrought or cast counterparts. In these strategies, AM allows fabrication of preform geometries without the need for custom tooling or feedstock. Conventional post-processing mitigates AM-specific issues such as anisotropic mechanical properties, residual stresses, porosity, and the presence of large columnar grains with pronounced texture. This study focuses on a hybrid AM-forging approach, in which the hot deformation behaviour of wire arc additive manufacturing (WAAM) processed Inconel 718 preforms was evaluated using hot compression tests (HCT). Cylindrical samples from WAAM deposited walls were hot compressed in a Gleeble® 3800 physical simulator at 927–1100 °C and strain rates of 0.01–5 s^{-1}. The evolution of microstructural anisotropy and flow behavior under these conditions was examined using optical microscopy (OM), field emission scanning electron microscopy (FE-SEM), energy dispersive spectroscopy (EDS), and electron backscatter diffraction (EBSD). Dynamic recrystallization (DRX) was dominant in specimens deformed at 5 s^{-1}, while dynamic recovery (DRV) prevailed at 0.01s^{-1}. The size of recrystallized grains during hot deformation was predicted using a phenomenological model based on the Zener-Hollomon parameter. The results revealed that grain size varies as a function of strain, enabling the tailoring of the grain structure of components forged from AM preforms. Processing maps indicated a power dissipation efficiency (η) of ~0.33 in a stable hot-working regime, consistent with DRX-dominated microstructural refinement.

1. Introduction

Metal additive manufacturing technologies have rapidly matured to the point where they are becoming suitable for manufacturing complex and high-performing parts, especially in the aerospace sector. These recent advancements enable the production of items with intricate geometries, reduced weight, and customized material properties, which were previously difficult or impossible with conventional manufacturing technologies. Additionally, metal additive manufacturing is also recognized for its potential to reduce fabrication process material waste to near-zero levels [1]. This development creates the potential for AM processes to be both more economical and energy efficient than traditional manufacturing processes such as conventional machining and forging [2].

Directed energy deposition (DED) is a technique used in wire arc additive manufacturing (WAAM). [3]. This process builds a component in a layer-by-layer process by concurrently melting and depositing metal wire onto a substrate using an electric arc. Because WAAM has greater deposition rates than powder-based manufacturing techniques, it can be used to rapidly construct large components. WAAM can produce near-net shape parts, reducing material wastage, lead times, and energy usage compared to traditional manufacturing processes like forging or casting. According to existing studies [4,5], fabrication of a Ti–6Al–4V external landing gear assembly using WAAM resulted in a material

* Corresponding author.
E-mail address: T.Borkar@csuohio.edu (T. Borkar).

https://doi.org/10.1016/j.jmrt.2025.12.213
Received 6 November 2025; Received in revised form 16 December 2025; Accepted 20 December 2025
Available online 23 December 2025

weight saving of up to 16.7 % per part for the exterior landing gear system. WAAM enables the fabrication of components from metallic systems that are traditionally challenging to process using conventional manufacturing routes. When applied to high-priced materials like nickel-base superalloys and titanium alloys, WAAM's potential cost-effectiveness is increased even further [5]. Specifically, the aerospace, energy, and advanced manufacturing sectors rely heavily on Inconel 718, a nickel-based superalloy, due to its remarkable fatigue resistance, corrosion resistance, and high-temperature strength [6,7]. These qualities allow it to continue to function mechanically at temperatures as high as 650 °C, making it essential for crucial parts such as pressure vessels, heat-resistant fasteners, and turbine blades [8].

While WAAM offers numerous advantages, the high peak temperatures, steep thermal gradients, and rapid solidification associated with the process can induce pronounced microstructural heterogeneities and processing defects in additively manufactured Inconel 718, which may significantly compromise its mechanical performance [5,9]. Regardless of these challenges, current research interest in WAAM processing of Inconel 718 is high [10,11].

WAAM-fabricated IN718 typically exhibits a microstructure characterized by a strong crystallographic texture, coarse columnar grains, and noticeable microstructural and chemical inhomogeneity along the build direction [12]. During WAAM, solidification and cooling processes frequently cause segregation of alloying elements, especially for niobium. This facilitates the formation of brittle Laves phases and large delta (δ) phase precipitates in the interdendritic areas and at grain boundaries [7,13,14]. Thus, AM-fabricated components may not reach the required levels of toughness, fatigue resistance, and strength, particularly at high temperatures, without significant subsequent post-processing.

To overcome these limitations, Alcoa Corporation proposed a process known as Ampliforge™, a hybrid manufacturing process where the AM process is combined with a forging post-processing step [15]. The mechanical properties of AMed components can be enhanced through subsequent forging. In this approach, the part is first designed and printed in a near-net-shape configuration, which then serves as the preform for the forging process. The schematic of this hybrid manufacturing for fabricating a wedge-shaped part is illustrated in Fig. 1. In this process, several conventional steps such as machining, annealing, rolling, and casting are eliminated, allowing the final component to be produced more quickly and at a lower cost [2]. Although forging adds an additional processing step, it preserves key advantages of AM such as the ability to fabricate near-net-shape preforms, reduce the buy-to-fly ratio, and eliminate the need for conventional billet-specific tooling [16].

This approach could be used to mitigate many of the microstructural issues present in metal additive material without introducing unintended shape changes, as reported in the open literature. However, much of the research has focused on the use of hot isostatic pressing (HIP). The reported literature on post-AM forging operations is sparse but merits more focus [2,17,18] due to the possibility that forging-induced recrystallization could convert anisotropic columnar grains into an equiaxed structure, providing grain refinement. HIP is typically utilized for pore closure and improvement of fatigue properties [19]. Blackwell [20] demonstrated that HIP processes can alleviate poor interlayer bonding and reduce anisotropy. Wycisk et al. [21] showed that post-treatment by HIP can reduce intrinsic defects and, as a result, significantly improve high-cycle fatigue performance. However, the HIP process is expensive in terms of supplies, machinery, and time. Alternatively, through isothermal hot compression testing, Roush et al. [22] enhanced the mechanical performance of laser-deposited Ti–6Al–4V in terms of microstructure patterns and anisotropy. Mostafa et al. [23] examined the mechanical properties of laser powder bed fusion (LPBF) processed Inconel 718 at elevated temperatures (1050 °C and 1150 °C) and strain rates ($0.1s^{-1}$ and $0.01s^{-1}$). They also examined microstructural changes with regard to grain size and crystallographic texture. Their findings demonstrated that hot compression produced finer, equiaxed grains and that mechanical behavior was more dependent on strain rate than temperature. Abedi et al. [24] presented additively manufactured Inconel 625 with a lower peak stress than the hot-forged material of the same composition. Sizova et al. [25] investigated the microstructure evolution of Ti–6Al–4V preforms, processed by selective laser melting (SLM), during heat treatment and hot working. In this study when compared to traditional wrought material with a lamellar microstructure, the results demonstrate that the as-built SLM samples are well hot workable, have a lower activation energy for hot working, lower peak stresses, and faster globularization kinetics. These characteristics may be used to decrease the tool load during forging and are also thought to be advantageous for hot working. A previous study on the hybrid additive manufacturing of 316L stainless steel reported that the columnar grains were transformed into equiaxed grains, accompanied by increases of approximately 27 % in yield strength and 32 % in ultimate tensile strength [26]. In addition, Recent developments in field-assisted and deformation-assisted AM show intriguing strategies to get around arc-based techniques' intrinsic microstructural constraints. It has been demonstrated that ultrasonic rolling-assisted wire arc DED greatly improves mechanical performance in IN718 by refining grains, suppressing Laves phase development, and randomizing texture [27]. While hybrid plasma-arc micro-rolling approaches similarly achieve substantial grain refinement, defect suppression, and improved γ'/γ'' precipitation strengthening under ~30 % in-situ deformation [28]. In addition to these advancements, a thorough analysis of field-assisted AM shows how adding thermal, mechanical, acoustic, and magnetic fields can actively modify solidification kinetics, melt-pool behavior, and defect evolution to enhance microstructure and characteristics [29]. Additionally, recent reviews emphasize that deep learning is increasingly enabling microstructure prediction, defect detection, process monitoring, and property optimization in metal AM, with physics-informed and real-time models offering new opportunities for intelligent, data-driven process control [30].

Forging complex components with high strain requirements often necessitates a large number of pre-forming steps (typically 2 to 7) to

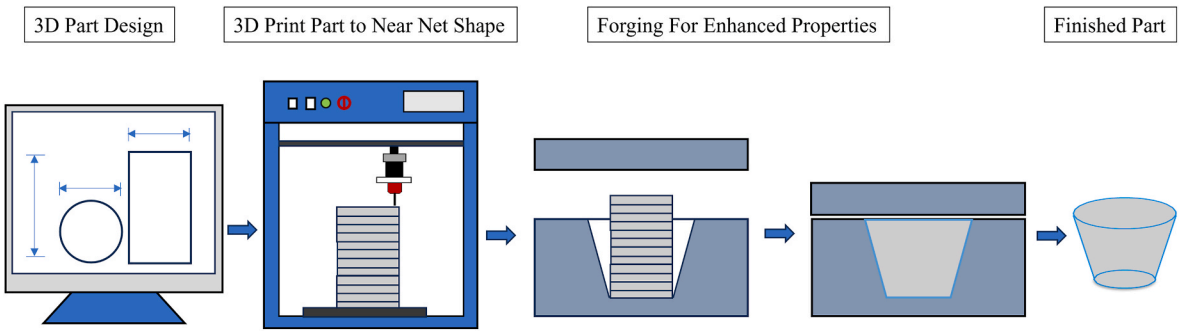

Fig. 1. Schematic illustration of Ampliforge™ process [15].

gradually shape the material, avoid defects, achieve the desired mechanical properties, and ensure uniform refinement of the internal structure. Although effective, this multi-step process approach leads to increased tooling costs and longer lead times, which can be challenging, especially for low-volume production. Additively manufactured preforms could bypass many of the preforming steps of the traditional forging process, reducing the number of required steps and, consequently, lead times, material, energy, and cost inputs. However, the design methodology for producing AM preforms with the desired grain structure, forgeability, dimensional accuracy, and mechanical properties is yet to be systematically and fully developed. The present work systematically investigates the high-temperature flow behavior, mechanical properties, and microstructure evolution of Arc-DED fabricated Inconel 718 superalloy during the hot deformation process. We focus on determining the optimum window of thermomechanical parameters, strain, temperature, and strain rate to generate homogenous forged microstructures from AM preforms. Furthermore, the study highlights the potential of hybrid manufacturing by integrating additive manufacturing with low-volume forging applications.

2. Materials and methods

2.1. Sample preparation by wire arc additive manufacturing (Arc-DED)

Inconel 718 wall was manufactured using a gas metal arc welding (GMAW)-based WAAM process (Gefertec Arc 600) as depicted in Fig. 2 (a). GMAW-based WAAM is a DED additive manufacturing technique that builds a metal component in a layer-by-layer fashion using an electric arc as the heat source and metal wire as the feedstock. The chemical composition of the 1.2 mm diameter wire (WB alloys) is shown in Table 1. The process parameters used are listed in Table 2 and Fig. 2 (b) shows the resultant IN718 wall structure (279.4 mm × 279.4 mm × 50.8 mm).

Hot compression test samples were extracted from the WAAM-processed wall at different locations, as presented in Fig. 2(c). First, the wall was cut into three sections (top, center, and bottom) by machining. Then, cylindrical samples were extracted by wire electric discharge machining (EDM, Mitsubishi, MC Machinery Systems Inc.) with a diameter of 12.7 mm and a length of 19.05 mm as shown in Fig. 2 (d).

2.2. Hot compression testing (HCT)

A Gleeble®3800 thermomechanical system was used to conduct the high-temperature compression testing. The test samples were deformed to a true strain value of 0.40, at strain rates of 0.01, 1, and 5 s^{-1}, and temperatures of 927, 1000, and 1100 °C (1 °C/s heating rate, 5-min pre-test hold), and then air quenched with compressed air to produce a cooling rate of approximately 35 °C/s post-test. The deformation temperatures of 927, 1000, and 1100 °C were chosen to hold a critical range for the material's hot workability [31–33]. The lower temperature (927 °C) is near the suspected recrystallization temperature, allowing for the investigation of deformation mechanisms, to design an AM preform at a lower temperature. The intermediate and higher temperatures (1000 and 1100 °C) represent common industrial forging windows, where dynamic recovery and dynamic recrystallization are the dominant softening mechanisms. Furthermore, prior studies report that the contribution of adiabatic heating to the overall deformation response diminishes at higher temperatures. Thus, employing low, intermediate, and high deformation temperatures enables a meaningful evaluation of the adiabatic heating effect across different thermal conditions. This temperature range is crucial for understanding the evolution of microstructure (e.g., grain refinement) and flow stress under practical processing conditions, before designing AM preform [33,34]. The strain rates were selected to simulate different types of industrial forging processes [35]: hydraulic (0.01s^{-1}), mechanical (1s^{-1}), and hammer forge (5s^{-1} or above) [36,37].

The HCT thermal profile is shown in Fig. 3, and the experimental setup of the Gleeble system is shown in Fig. 4(a). Three thermocouples were affixed to the middle of the cylinder and approximately 3 mm from both ends of the specimen, as illustrated in Fig. 4(b). The middle thermocouple was used as the control signal while the other two served as references. A temperature difference of 5–7 °C was observed between the central and edge thermocouples.

To reduce friction between the sample and anvil surfaces, a combination of tantalum foil (0.1 mm) and nickel-based grease was utilized, as

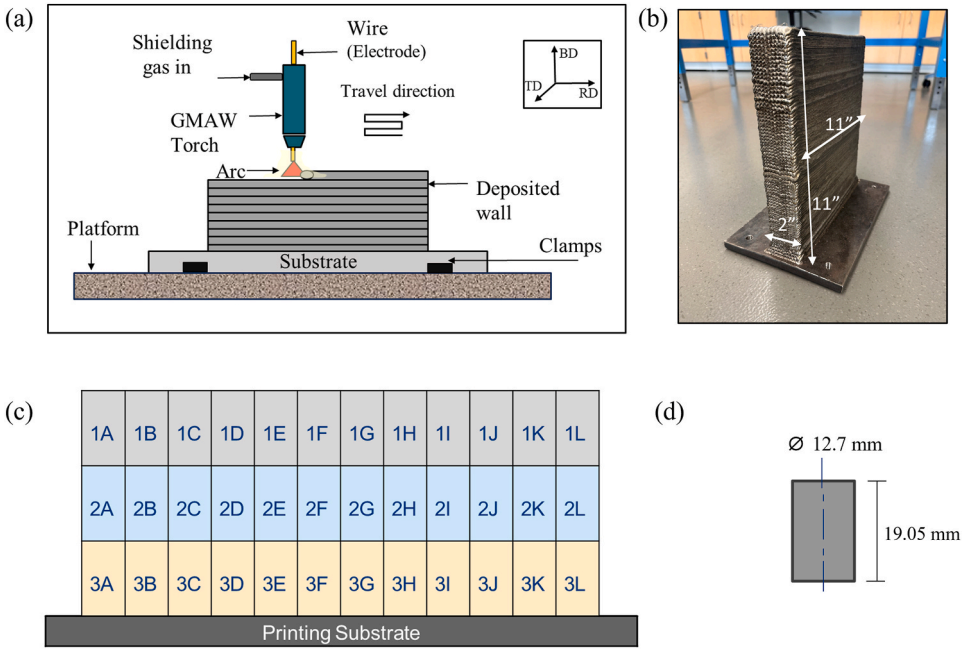

Fig. 2. (a) Schematic illustration of the WAAM process, (b) Inconel 718 Wall, (c) Hot compression test (HCT) sample preparation process, (d) HCT sample dimensions.

Table 1
Wire chemical composition of Inconel 718 used for WAAM (wt.%).

Element	Ni	Cr	Fe	Nb	Mn	Ti	Cu	S	P	C	Si
Wt. %	>67	18–22	<3	2–3	2.5–3.5	<0.75	<0.5	<0.015	<0.015	<0.05	<0.5

Table 2
GMAW-WAAM process parameters used for fabricating Inconel 718.

Parameter	Wire Diameter (mm)	Current (A)	Voltage (V)	Wire Feed Speed (m/min)	Travel Speed (mm/min)	Shielding Gas Flow (L/min)
Level	1.2	156–175	13.4–14.9	5.6–7	900–1080	15

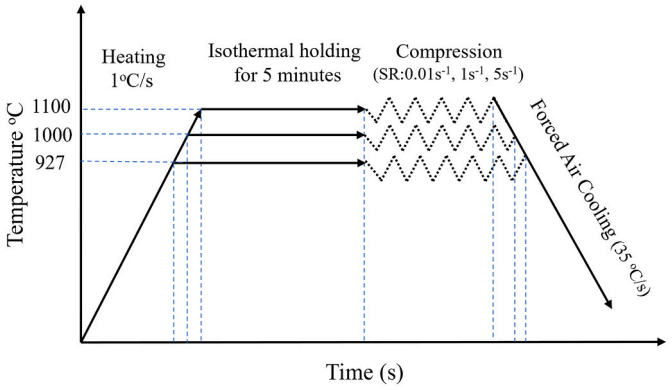

Fig. 3. Thermal cycle graph showing the heating, isothermal hold, hot compression and cooling testing cycle.

shown in Fig. 4(c). The force applied to the specimen and the change in length of the sample during hot compression experiments were monitored using a load cell and L-gauge, respectively. The measured load-displacement data were used to calculate true stress-strain curves.

2.3. Microstructure analysis

The hot deformed samples were cut at the center along the deformation axis by wire electric discharge (EDM, Mitsubishi, MC Machinery Systems Inc.). The samples were hot-mounted and ground to 1200 grit using silicon carbide (SiC) media, with water serving as both a coolant and lubricant. Colloidal silica (0.04 μm) was utilized as a final polishing step, followed by ultrasonic bath cleaning. Further surface preparation was utilized for electron beam backscatter diffraction imaging, including vibratory polishing.

Microstructural examinations and elemental analysis were performed using a scanning electron microscope (SEM, FEI Inspect F50, USA) equipped with an energy dispersive X-ray spectroscopy (EDS) system (Oxford Instruments XMAX). Electron beam backscatter

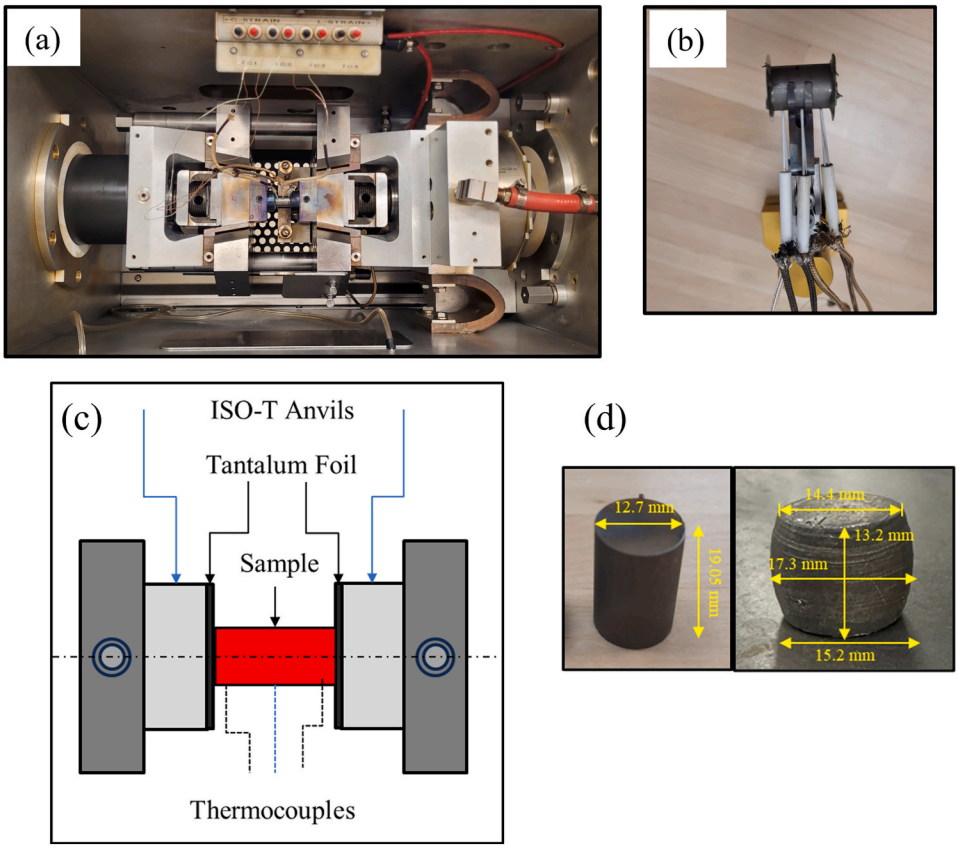

Fig. 4. (a) Compression test setup inside the Gleeble chamber, (b) thermocouple placement, (c) schematic of experimental setup with sample, thermocouples and anvils and (d) cylindrical test sample before (left) and after (Right) deformation.

diffraction analysis was performed on a JSM-7900F scanning electron microscopy equipped with an EDAX Hikari + system. ImageJ software was utilized for grain size measurement and distribution analysis.

3. Results and discussion

3.1. Initial microstructure of WAAM-processed Inconel 718

As-deposited optical and SEM micrographs shown in Fig. 5 indicate that grains in the YZ plane (parallel to the build direction) are both columnar and relatively coarser. The average grain size of the WAAM as-fabricated sample in the YZ plane was measured as 438 μm. The optical images presented in Fig. 5(a) and (b) reveal clear evidence of dendritic and interdendritic structures. Fig. 5(c) shows a columnar dendritic structure aligned along the build direction, formed due to directional solidification under high thermal gradients. The black spots are most likely oxide inclusions, pores. During WAAM, localized oxidation and gas entrapment can occur due to the high heat input and molten pool exposure to air, forming small pores or oxide particles (e.g., Al_2O_3, TiO_2, Nb-oxides). During layer-by-layer processing, the grains expand across the deposited layers [33]. To further confirm these black spot a EDS spot analysis is carried out, and the corresponding energy spectrum is shown in Fig. 5(e), and composition is listed in Table 3 (Spot 1), the high % of O_2 and Si confirms oxide rich inclusions. However, due to variations in local solidification velocity, there is an interlayer variation, with coarser dendritic structures in the top layer and finer cellular grains in the bottom layer [38,39]. Nb/Ti-rich laves phases are dispersed across columnar dendritic arms and are produced by micro segregation during solidification, as shown in Fig. 5(d). To verify the presence of the Nb/Ti-rich intermetallic phase, an additional EDS spot analysis was performed on the bright interdendritic region. The energy spectrum is provided in Fig. 5(f), and the quantified elemental composition is presented in Table 3 (Spot 2). The significantly enriched Nb (11.13 at. %, 20.78 wt%) and Ni–Ti–Cr balance are consistent with the composition typically reported for the Nb/Ti-rich Laves phase in additively manufactured Inconel 718 [40]. Similar initial microstructures are reported by other studies of additively manufactured nickel-based superalloys [23,33,41–43]. Cellular structures were also observed in as-fabricated IN718, as shown in Fig. 5(d). To melt the wire feedstock and create a large molten pool, the WAAM process requires a substantial amount of heat input. The resultant slow cooling rate (10^1–10^3 K/s) [44] during solidification promotes the development of cellular and columnar dendritic structures. In addition, columnar and cellular crystals are more likely to form during WAAM because of the directional heat flow that causes grains to grow in the build direction. Additionally, elemental segregation occurs, promoting the formation of laves phases and carbides, which further contribute to the cellular or dendritic microstructure [12,33,45,46]. The Laves phase and poorly managed carbide formation considerably degrade the mechanical performance of WAAM fabricated parts, but can be addressed through homogenization treatments prior to aging and hot deformation processes [12,33].

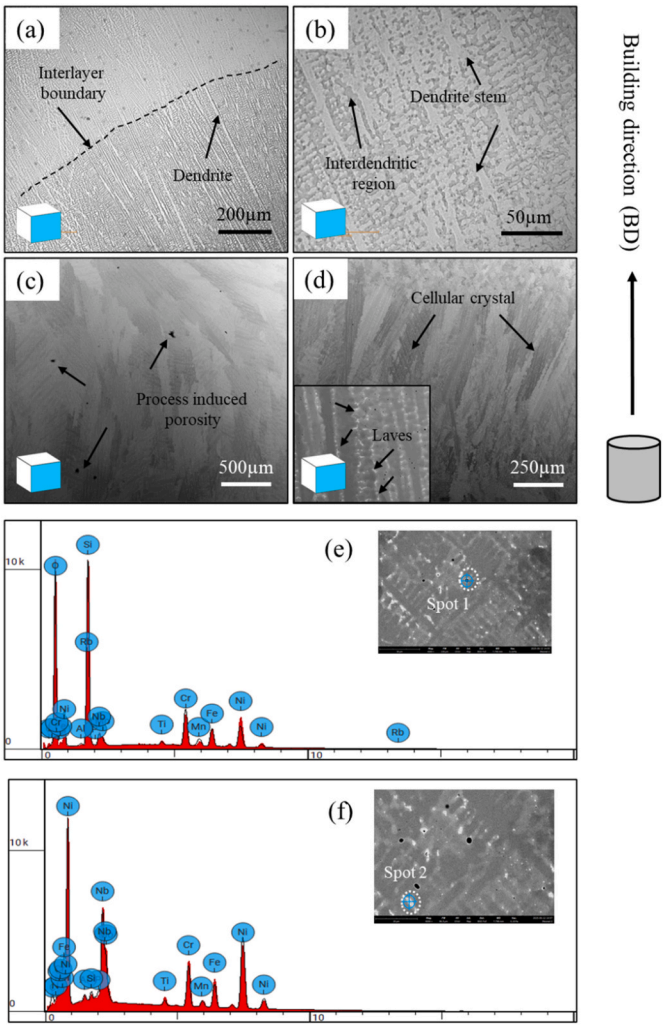

Fig. 5. As-deposited IN718 microstructure processed by wire arc additive manufacturing (a, b) low and high magnification optical micrographs, (c,d) low and high magnification SEM micrographs, showing elongated grain growth in the build direction in some regions, and small equiaxed microstructires in others(e) EDS spectrum of the oxide inclusion; (f) EDS spectrum of the bright Nb/Ti-rich phase.

3.2. Effect of deformation conditions on flow stress behavior

Flow stress curves were obtained from hot compression tests at different temperatures and strain rates. Examples of the resulting experimental true stress-true strain curves, for WAAM fabricated IN718 at various temperatures and strain rates, are shown in Fig. 6. Flow stress behavior obtained at different strain rates exhibited similar trends irrespective of temperature. Microstructure evolution and flow stress change are typically attributed to two competitive phenomena: work hardening (WH) and diffusion-based behavior.

Increasing the deformation temperature from 900 to 1100 °C substantially reduced the peak flow stress value. This softening effect is attributed to enhanced atomic mobility and the activation of DRV and DRX softening mechanisms. The energy barrier for dislocation movement falls at higher temperatures, which slows work hardening rates and promotes microstructural evolution. In line with the commencement of DRX, a shift from strain hardening to strain-softening behavior was observed, especially at 1100 °C. However, because of its

Table 3
Chemical composition (EDS) of inclusion and Laves phase identified in Fig. 5.

Element	Spot 1			Spot 2		
	Atomic %	Weight %	Bulk %	Atomic %	Weight %	Bulk %
O	50.032	25.574	–	3.107	0.999	–
Al	0.232	0.200	0.2–0.8	1.106	0.599	0.2–0.8
Si	18.145	16.284	<0.5	0.885	0.500	<0.5
P	0.101	0.100	<0.015	0.802	0.500	<0.015
Ti	0.522	0.799	<0.75	0.934	0.899	<0.75
Cr	8.780	14.585	18–22	10.708	11.189	18–22
Mn	0.968	1.698	2.5–3.5	0.452	0.500	2.5–3.5
Fe	5.543	9.890	<3	7.656	8.591	<3
Ni	10.976	20.579	>67	39.900	47.053	>67
Nb	1.548	4.595	2–3	11.130	20.779	2–3
Mo	0.424	1.299	–	1.554	2.997	–

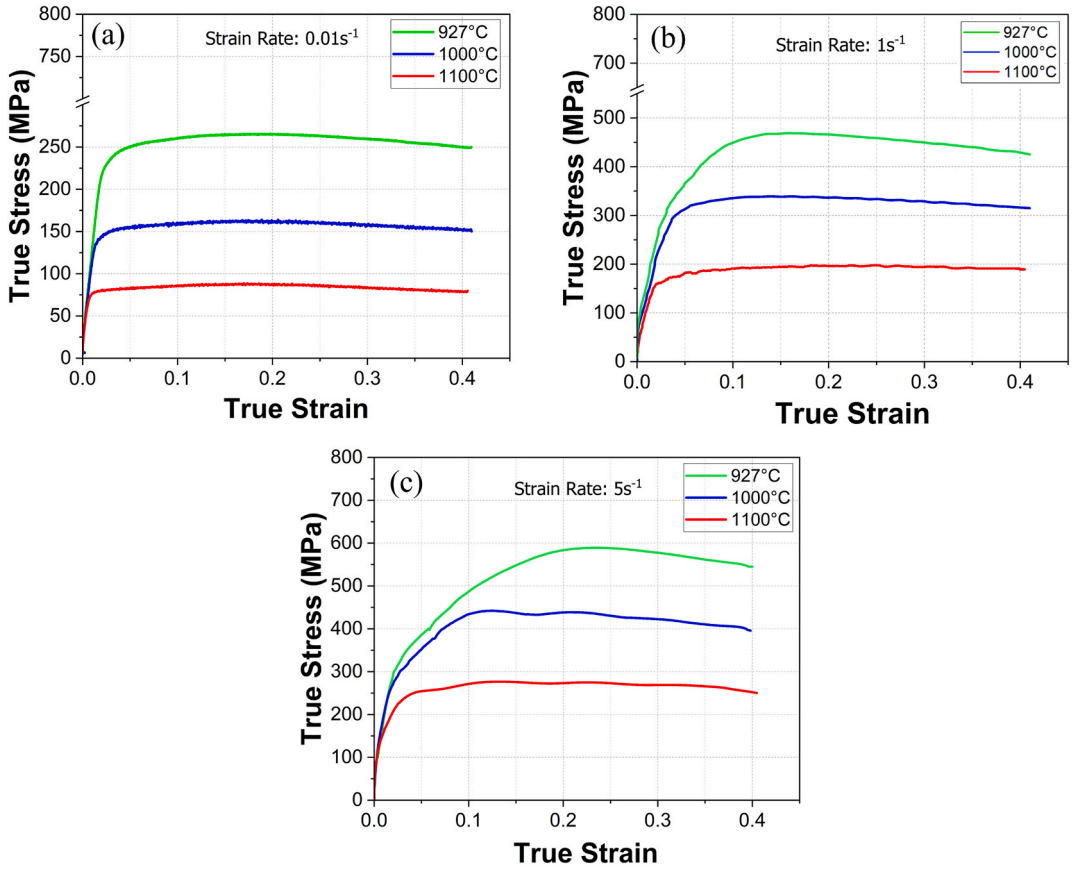

Fig. 6. Flow behavior of WAAM IN718 at different temperatures (927°C, 1000°C, 1100°C) and strain rate of (a) 0.01s^{-1}, (b) 1s^{-1}, and (c) 5s^{-1}.

comparatively low stacking fault energy (SFE, 50–75 mJ/m^2) [24,47], IN718 alloy experiences less softening during dynamic recovery, and the high dislocation density encourages the development of DRX [2,25]. Furthermore, at a constant deformation temperature, the flow stress gradually decreases with increasing strain, whereas an increase in strain rate leads to a corresponding rise in flow stress, as previously reported by other authors for Ni-based superalloys [23,48,49]. This effect is primarily due to the increased time available for dislocation annihilation at lower strain rates, which facilitates dynamic recovery and results in significantly lower flow stress compared to that observed at higher strain rates. Work hardening was observed at the beginning of all compression tests, resulting in a monotonic increase in flow stress. However, dislocation density then decreases as DRV phenomena are activated. DRX counteracts the work hardening at a critical strain value, resulting in a flow curve peak followed by softening processes, which dominate until a stable state is achieved, with work hardening and dynamic softening processes in near-equilibrium [2,50].

During these hot deformation processes, lower strain rate and higher deformation temperature result in the lowest strength. This behavior is likely explained by the time and energy required for nucleation and the development of new dynamically recrystallized grains, which are suppressed at lower temperatures and/or higher strain rates [3].

Flow stress behavior is depicted in Fig. 7 as a plot of maximum flow stress vs. temperature and strain rate. A maximum flow stress value of 589 MPa was observed at 927 °C and 5 s^{-1}, while the minimum flow stress value of 88 MPa occurred at 1100 °C and 0.01 s^{-1}, highlighting the combined effect of temperature and strain rate on hot deformation behavior of IN718.

The activation energy for hot compression (Q) was computed using the Arrhenius technique [51,52]. The Zener Hollomon parameter (Z) was used to express the combined effect of strain rate and temperature on flow stress behavior:

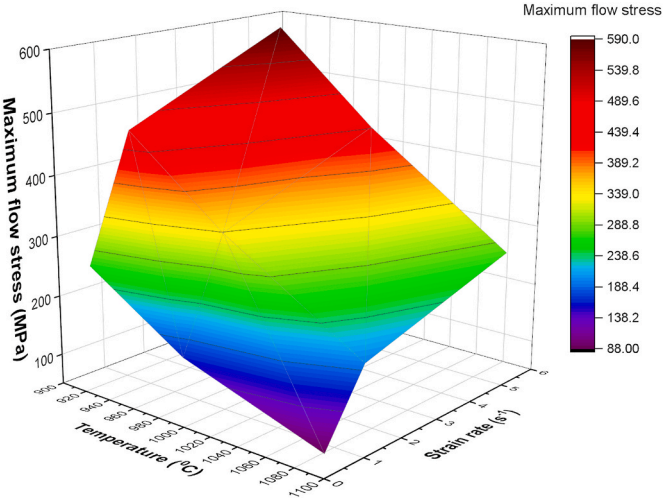

Fig. 7. Effects of temperature and strain rate on the maximum flow stress value during hot deformation of IN718.

$$Z = \dot{\varepsilon} exp\left(\frac{Q}{RT}\right) \quad (1)$$

Where R is the universal gas constant (8.314 J/mol K), Q is the activation energy (J/mol); $\dot{\varepsilon}$ is the strain rate (s^{-1}); and T is the deformation temperature (K). It is also possible to use various constitutive models, such as the power law, exponential law, or hyperbolic sine law, to depict the Zener-Hollomon parameter (Z) as a function of stress.

$$z = \begin{cases} A\sigma^{n'} & (\alpha\sigma)<0.8 \\ A\,exp(\beta\alpha) & (\alpha\sigma)<1.2 \\ A[sinh(\alpha\sigma)]^{n} & \text{For all } \sigma \end{cases} \quad (2)$$

Where A, β, n, n' and α are material constants. For low and moderate stress levels, the power relationship is typically recommended [2]. The exponential equation applies at high stresses, where power law breakdown occurs. Alternatively, an Arrhenius-type equation utilizing the hyperbolic sine rule can often be used, with sufficient accuracy, over a broad range of temperatures and strain rates [51]. This latter approach was utilized for analysis. The material constants were calculated from data taken at a constant true strain value. In the low and high stress regimes, the following two expressions were utilized for substitution into equation (1):

$$\dot{\varepsilon} = B\sigma^{n'} \quad (3)$$

$$\dot{\varepsilon} = C\,exp(\beta\alpha) \quad (4)$$

Where B and C are material constants. Solving equations (3) and (4) by taking the log of both sides and linear fitting of ln(strain rate) vs true stress and ln(σ), the values of β and n' were determined to be 0.027 MPa^{-1} and 6.64, respectively. Therefore, the value of α can be calculated as:

$$\alpha = \frac{\beta}{n'} = 0.004066 \quad (5)$$

Substituting the hyperbolic form in equation (2) into equation (1) and taking the logarithm of both sides results in the following equation:

$$ln[sinh(\alpha\sigma)] = \frac{ln\dot{\varepsilon}}{n} + \frac{Q}{nRT} - \frac{ln\,A}{n} \quad (6)$$

From the slope of the line $ln\ (strain\ rate)$ vs $ln\ [Sinh(\alpha\sigma)]$ n computed to be 6.6430. Then Q is calculated using the linear relationship between $ln[sinh(\alpha\sigma)]$ and $1/T$, resulting in 496.865 kJ/mol. This value was calculated for a true strain value up to 0.4, to create a plot of activation energy vs strain. The average activation energy was calculated to be 472.05 kJ/mol. This value is higher than that reported for wrought materials. The hot deformation activation energy for wrought IN718, in the same temperature range, is reported as 423–458 kJ/mol [53]. In another paper, the mean activation energy for high-temperature forming at 900–1150 °C was reported as 450.8 kJ/mol for IN718 and 412.7 kJ/mol for INX750 [54]. Thus, based on the results discussed earlier, we conclude that WAAM-processed IN718 exhibits more resistance to deformation at elevated temperatures than wrought IN718, likely due to the presence of solidification-induced microstructural heterogeneities, elemental segregation, and thermally induced residual stresses during layer-by-layer fabrication. The combined effect of these characteristics raises the energy needed for hot deformation by impeding dynamic softening processes. This is further discussed in the microstructure evolution section. It should also be noted that the activation energy increases as the geometrically necessary dislocations (GNDs) increase. This means that the activation energy likely reflects the amount of energy required to facilitate the movement of dislocations during the hot deformation.

3.3. Microstructure evolution during hot compression testing

The samples were macro-etched using Kalling's Reagent No. 2 for 10 s, and optical macrographs were acquired using a Keyence VHX-1000 digital microscope. Fig. 8 illustrates the deformation bands and material flow under different deformation conditions, temperatures, and strain rates, all at the same level of strain. The deformation conditions selected for the macroscopic images in Fig. 8 were chosen to systematically capture the combined influence of temperature and strain rate on hot deformation behavior; while remaining relevant to industrial

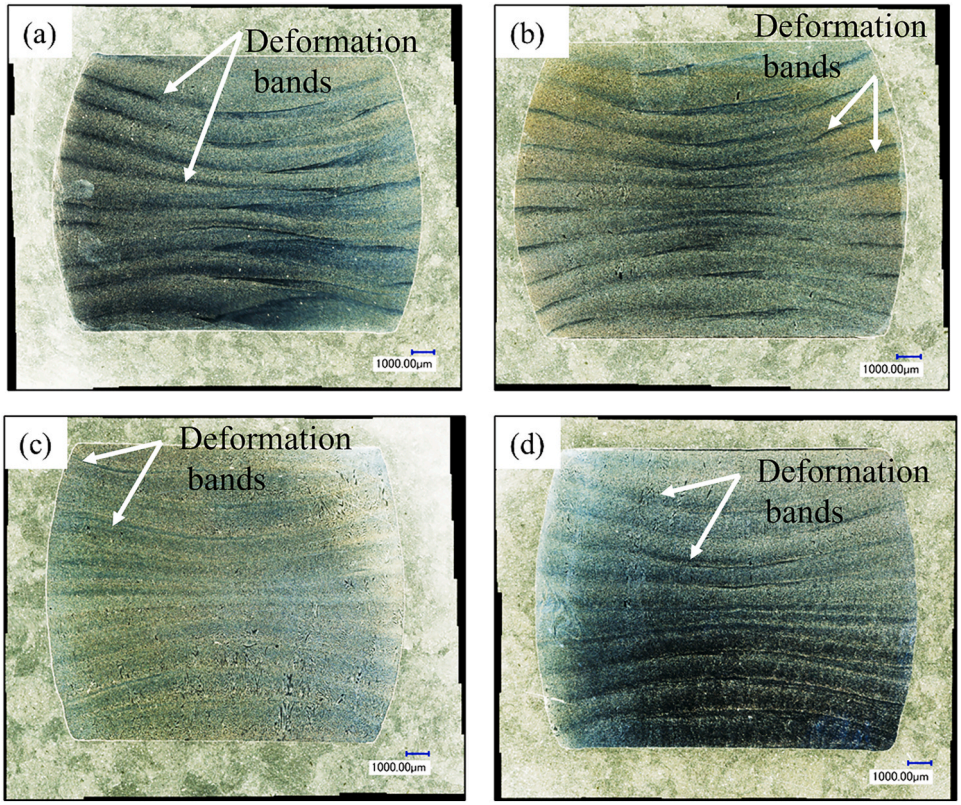

Fig. 8. Represents macroscopic images with deformation bands after the hot deformation of WAAM 718 specimens at (a) 927 °C, 0.01 s-1, (b) 1000 °C, 0.01 s-1, (c) 11100 °C, 0.01s-1, and (d) 1000 °C, 5 s-1.

forging practice and AM preform design. The macroscopic deformation patterns clearly demonstrate a strong dependence on both temperature and strain rate. At lower deformation temperatures, the specimens exhibit more pronounced and closely spaced flow bands (Fig. 8(a)), indicating higher flow stress, limited dynamic softening, and an increased tendency for strain localization, particularly under high strain-rate conditions (5 s^{-1}), as shown in Fig. 8(d). With increasing deformation temperature, the flow lines become smoother, broader, and more uniformly distributed across the cross-section (Fig. 8(c)), reflecting enhanced dynamic recovery and dynamic recrystallization. At a given temperature, reducing the strain rate to 0.01 s^{-1} results in more homogeneous material flow and reduced band intensity, whereas increasing the strain rate to 5 s^{-1} leads to sharper band contrast and more heterogeneous deformation. This behavior is attributed to insufficient time for softening mechanisms and the influence of adiabatic heating. Overall, higher temperatures combined with lower strain rates promote stable deformation and uniform flow, while lower temperatures and higher strain rates favor localized deformation and flow instability.

Metallographic images showing the complex microstructural evolution of WAAM-processed Inconel 718 after hot compression testing are shown in Fig. 9. Across this range of temperatures and strain rates, microstructural transformations and phase changes are likely to occur. Before hot deformation, the samples were subjected to an isothermal hold for 5 min to ensure uniform temperature distribution and to stabilize the initial microstructure. SEM observations revealed that, at all test temperatures, the microstructure was dominated by columnar grains, indicative of the solidification texture inherited from the fabrication process. This columnar morphology suggests limited bulk recrystallization during the holding period, with grain growth occurring preferentially along the build or heat flow direction. Such a retained columnar structure can significantly influence subsequent deformation behavior, including the activation of slip systems, dynamic recovery, and dynamic recrystallization during hot compression. Quantitative grain size analysis was performed on the samples after the 5-min isothermal holding. The average grain size was found to increase slightly with temperature, measuring 448 μm at 927 °C, 457 μm at 1000 °C, and 465 μm at 1100 °C, indicating minimal grain coarsening during the holding period. The average recrystallized grain size of WAAM-processed Inconel 718 after hot deformation, shown in Fig. 10, exhibited distinct dependencies on both temperature and strain rate. At 927 °C, grain size varied from 3.2 μm at 0.01s^{-1} to 1.8 μm at 1s^{-1}, and 2.3 μm at 5s^{-1}. The presence of larger grains at lower strain rates is attributed to extended deformation time, which allowed for most post-dynamic recrystallization (post-DRX) grain growth. In contrast, the finest grains at 1s^{-1} suggest an optimal balance between DRX nucleation and growth. In contrast, the slightly larger grains at 5s^{-1} indicate incomplete recrystallization due to limited time for grain boundary

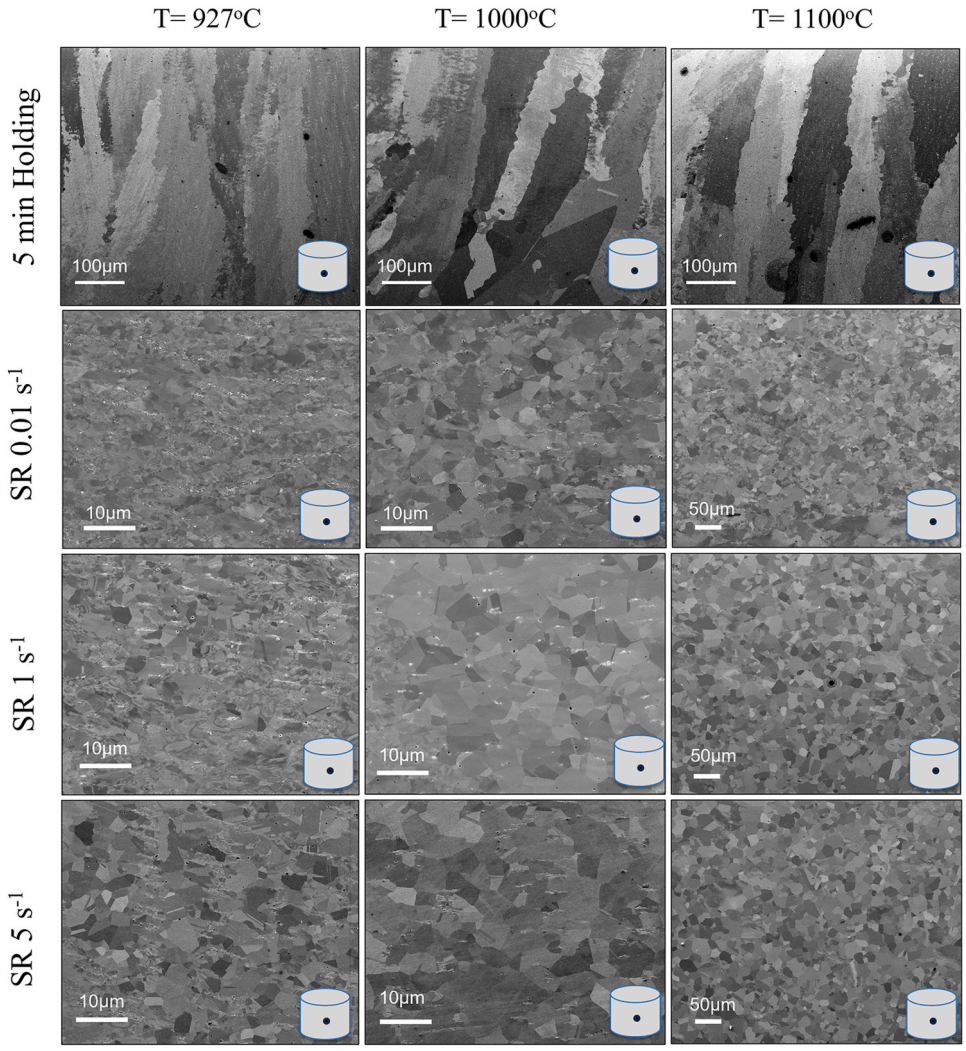

Fig. 9. SEM micrographs of HCT samples along compression direction after 40 % deformation: microstructural evolution variation with strain rates and temperatures. Grain size depends strongly on strain rate at low temperatures, while grain coarsening appears to be the controlling factor at elevated temperatures.

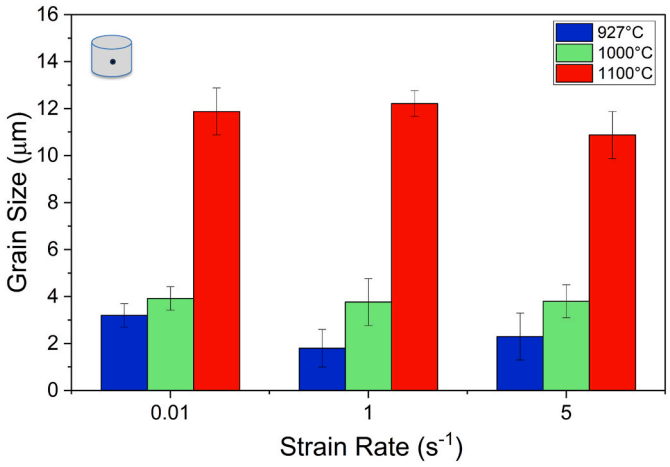

Fig. 10. Grain size analysis of hot deformed samples from FE-SEM micrographs.

migration. At 1000 °C, grain size differences across strain rates were minimal, with values of 3.92, 3.77, and 3.80 μm for 0.01, 1, and 5s^{-1}, respectively, suggesting that DRX rapidly reached a steady-state grain size where nucleation and growth rates were balanced. At 1100 °C, significantly coarser grains were observed: 11.88 μm at 0.01s^{-1}, 12.22 μm at 1s^{-1}, and 10.88 μm at 5s^{-1} due to the high grain boundary mobility and rapid grain growth promoted by elevated temperatures. The slightly smaller grains at 5s-1 reflect reduced grain growth time despite the overall dominance of thermal effects. These results demonstrate that strain rate influences grain size distribution at lower temperatures due to the DRX phenomena, while temperature becomes the controlling factor at elevated conditions, leading to pronounced grain coarsening.

Two representative sets of samples were selected for further electron beam backscatter (EBSD) analysis. In the first set, low and high strain rates at 1000 °C were considered, while in the second set, low (927 °C) and high temperatures (1100 °C) with a strain rate of 0.01 s^{-1} were examined. The selection condition was based on the highest and lowest flow stress values observed from the hot deformation tests.

EBSD scans were conducted along the longitudinal axis at the top, center, and bottom positions, as shown in the inset at the lower corner of

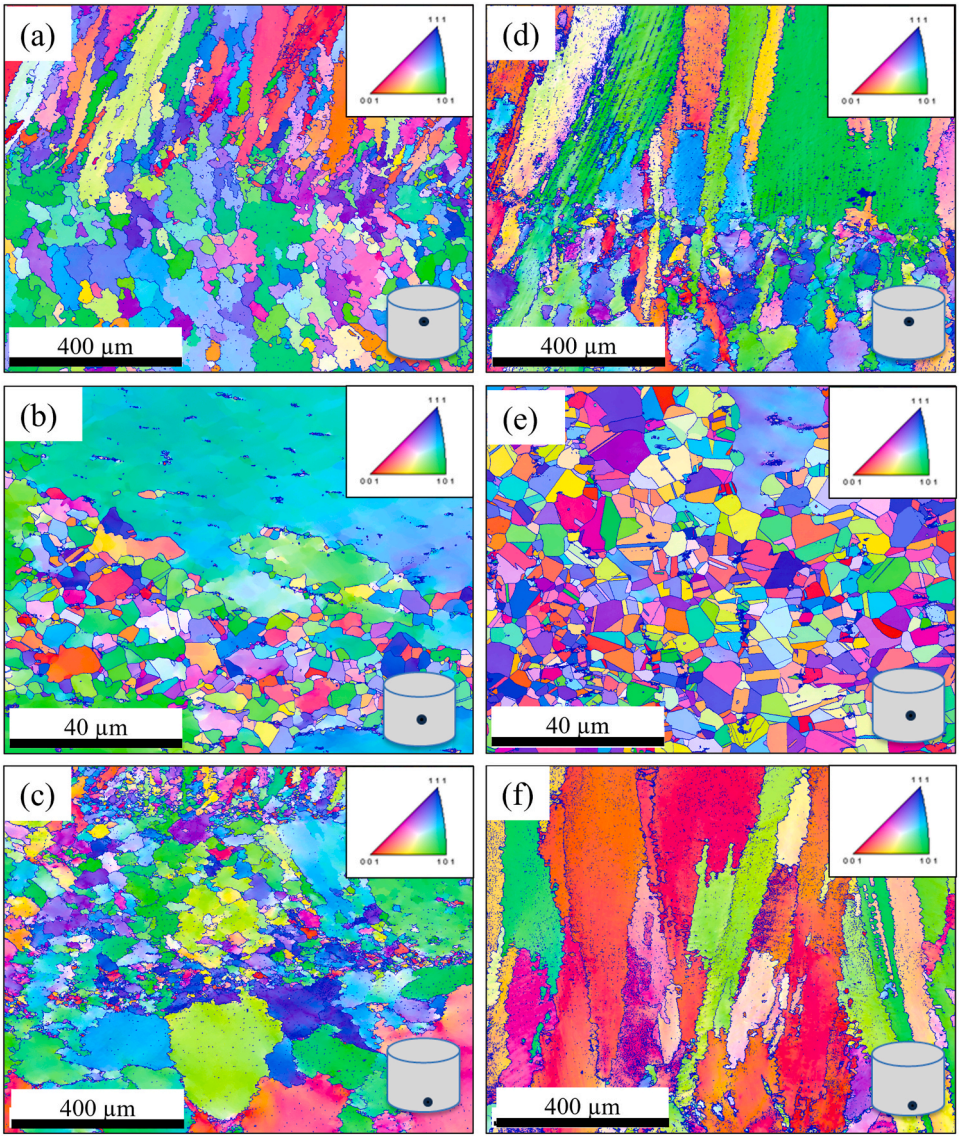

Fig. 11. EBSD maps of the HCT sample deformed at 1000 °C, showing the Top, Center, and Bottom regions: (a–c) at 0.01 s^{-1} and (d–f) at 5 s^{-1}, showing less dynamic recrystallization near platen surfaces and heterogeneous final microstructures.

the micrographs in Figs. 11 and 14. Fig. 11 presents EBSD inverse pole figure (IPF) maps of the HCT sample deformed at 1000 °C at two different strain rates, illustrating the microstructural variations along the top, center, and bottom regions of the specimen. The corresponding quantitative area grain size distribution is shown in Fig. 12.

Fig. 11(a–c) displays the resulting microstructures at a lower strain rate value of $0.01s^{-1}$, indicating a heterogeneous mixture of coarse elongated grains aligned along the deformation direction and fine equiaxed dynamically recrystallized (DRX) grains. The top and bottom region, Fig. 11(a) and (c), contain partially recrystallized areas interspersed with elongated grains, likely due to a combination of platen friction and temperature variation, resulting in a relatively large average grain size of 80.68 μm and 129.79 μm. The center region, Fig. 11(b), exhibits the finest grains (34.0 μm) and a more uniform distribution of equiaxed grains, suggestive of a higher extent of DRX due to greater local strain accumulation. However, Fig. 11(b) also shows a large grain with developing cellular structures, suggesting of a region on the cusp of dynamic recrystallization. The bottom region, Fig. 11(c), displays mixed coarse and fine grains (129.79 μm), suggesting strain inhomogeneity and incomplete DRX.

At the higher strain rate value of $5s^{-1}$, Fig. 11(d–f) shows a more pronounced variation in grain size. The center region, in Fig. 11(e), shows an extremely fine grain size (5.58 μm), corresponding to a highly refined and equiaxed DRX microstructure. In contrast, the top Fig. 11(d) and bottom Fig. 11(f) regions display very coarse grains, 198.17 and 249.81 μm, respectively. The microstructures are dominated by elongated grains and show limited DRX due to interface friction and less deformation during HCT, especially Fig. 11(f) which shows the least evidence of DRX, likely due to the variable nature of the grain structure. This behavior suggests that, at high strain rates, higher stored energy promotes rapid nucleation and refinement in high-strain zones (center), while reduced local strain and faster deformation kinetics at the edges suppress DRX and encourage grain coarsening. From an AM forging preform design perspective, the EBSD observations at 1000 °C reveal critical implications for tailoring deformation conditions to achieve grain refinement after forging. When combined with hot compression testing results, this data shows grain size and microstructure variation as a function of strain, allowing for targeted and tailored grain structure in forging using AM preforms.

Fig. 13 shows the (001) pole figures with respect to the EBSD maps in Fig. 11 for the sample deformed at 1000 °C at two strain rates ($0.01s^{-1}$ and $5s^{-1}$) in the top, center, and bottom regions. The texture intensity values represent maximum multiples of a random distribution (mrd) and distribution patterns provide further insight into the deformation and recrystallization behavior revealed in microstructural analysis. At $0.01s^{-1}$, the top region Fig. 13(a) exhibits a moderate texture intensity (max ~5.64mrd), with spread-out poles indicating partial randomization due to ongoing dynamic recrystallization (DRX). The center region Fig. 13(b) shows a stronger intensity (max ~10.95mrd) but with a broader pole spread, reflecting the presence of fine equiaxed grains (34.0 μm) and a relatively high fraction of DRX. The bottom region of Fig. 13(c) presents a comparably strong texture (max ~10.05mrd), with poles clustered along preferred orientations, consistent with the mixed elongated equiaxed grain structure and incomplete DRX seen in EBSD Fig. 13(c).

At $5s^{-1}$, the top region Fig. 13(d) retains a high texture intensity (max ~10.77mrd) with pronounced orientation clustering, in agreement with the coarse elongated grains (198.17 μm) and limited DRX observed in EBSD Fig. 11(d). The center region Fig. 13(e) shows a much weaker texture (max~2.37mrd) with diffuse pole distribution, reflecting the highly refined DRX microstructure (5.58 μm grain size) produced by high local strain and stored energy. The bottom region in Fig. 13(f) exhibits the strongest texture of all (max ~ 13.26mrd), dominated by sharp orientation clustering, which correlates with the coarse, deformation-aligned grains (249.81 μm) and suppressed DRX in EBSD Fig. 11(f). Additionally, the variable deformation and recrystallization instances in each location can account for the variance in texture intensity across the specimen compressed at 1000 °C under various strain rates. Because it undergoes the most uniform deformation and has the largest stored energy at the low strain rate of $0.01\ s^{-1}$, the central region produces the strongest texture, encouraging progressive but incomplete dynamic recrystallization. This results in a microstructure that is fine and partially recrystallized, but it still has enough deformation substructure to sustain a somewhat robust texture. In contrast, the top and bottom regions undergo reduced effective strain due to frictional and thermal gradients near the platens, leading to mixed elongated equiaxed grains and lower overall texture intensity. At the high strain rate of $5\ s^{-1}$, deformation behavior changes markedly: the center region undergoes intense local strain and adiabatic heating, resulting in rapid and extensive DRX that produces very fine equiaxed grains and consequently the weakest texture among the three regions. Meanwhile, the top and bottom regions exhibit more limited DRX because of restricted strain accommodation and larger thermal gradients near the platens, preserving deformation-aligned grains and producing stronger, more clustered textures particularly in the bottom region.

The EBSD inverse pole figure (IPF) maps in Fig. 14 illustrate the microstructure evolution of the HCT sample deformed at a strain rate of $0.01s^{-1}$ under two different temperatures (927 °C and 1100 °C), highlighting distinct grain size and morphology variations across the Top, Center, and Bottom regions shown in Fig. 15.

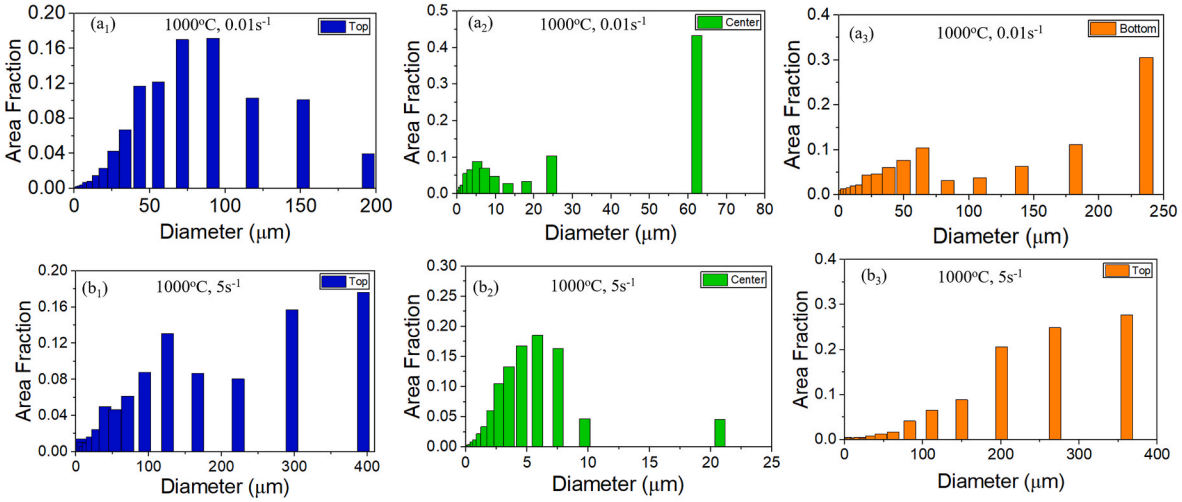

Fig. 12. EBSD grain size distribution of HCT samples deformed at 1000 °C, showing the Top, Center, and Bottom regions: (a_1-a_3) at 0.01 s-1 and (b_1-b_3) at 5 s-1.

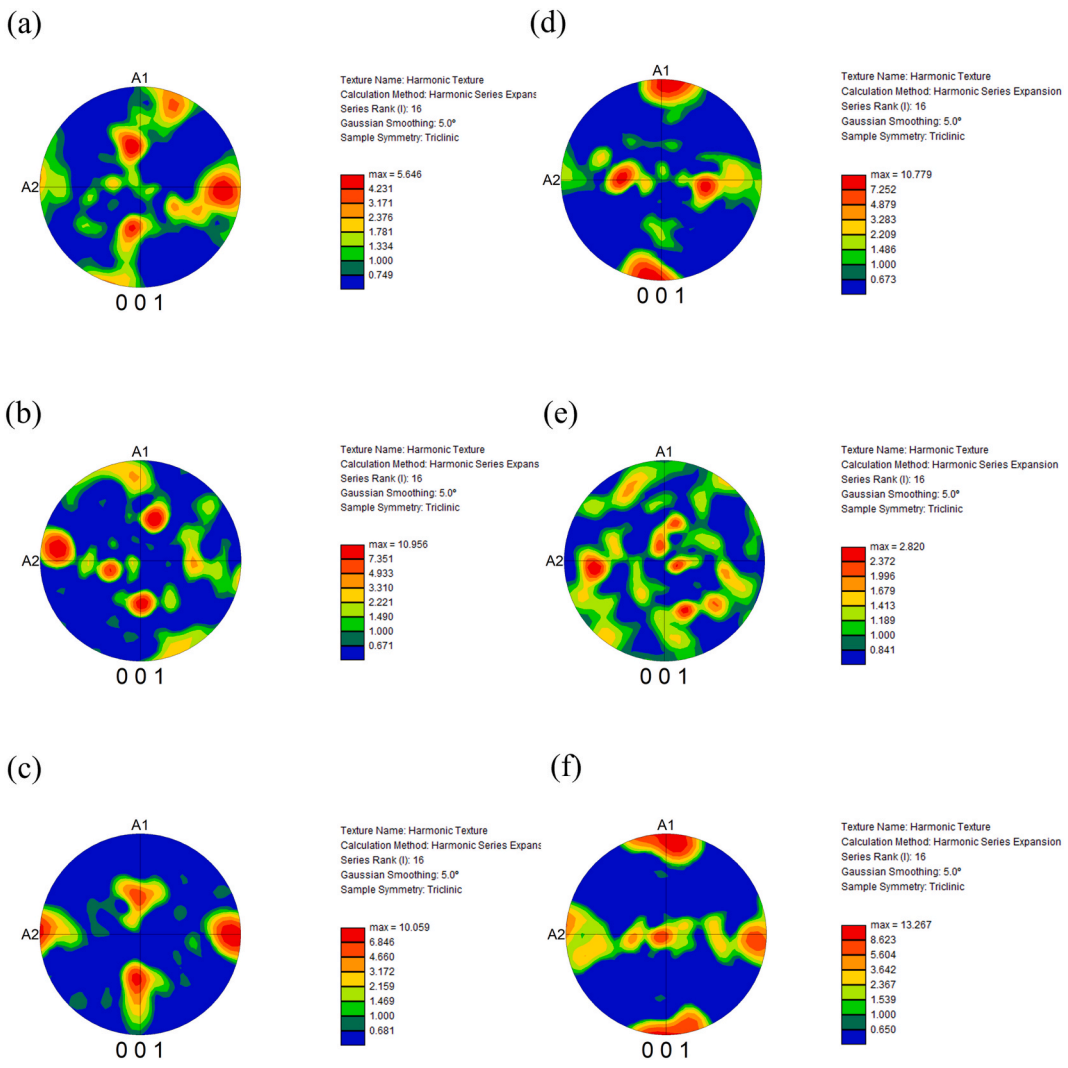

Fig. 13. Pole figures of HCT samples deformed at 1000 °C under strain rates of 0.01 s^{-1} (a–c) and 5 s^{-1} (d–f), showing (a, d) Top, (b, e) Center, and (c, f) Bottom regions.

At 927 °C (Fig. 14(a)–(c)), the top region exhibits coarse grains (area average of 206.74 μm), due to lower strain level and platen friction, indicating limited dynamic recrystallization (DRX), while the center shows a refined microstructure (area average of 28.48 μm), suggesting DRX due to high strain localization. The Bottom region displays an intermediate grain size (155.57 μm), consistent with partial DRX and a strain gradient across the sample. When the temperature is increased to 1100 °C (Fig. 14(d)–(f)), the center region undergoes notable grain coarsening (area average of 41.81 μm) due to grain growth at higher temperature, reflecting enhanced DRX and grain boundary mobility, while the top and bottom regions maintain relatively coarse but slightly refined grains (area average of 191.82 and 163.92 μm, respectively) due to low strain and platen friction. This microstructural evolution highlights the competing effects of strain localization and temperature-dependent DRX, where higher temperatures promote more homogeneous recrystallization but also facilitate grain growth.

The pole figures in Fig. 16 reveal distinct texture characteristics in the HCT sample deformed at 0.01s^{-1}, with notable differences between the top, center, and bottom regions at both 927 °C and 1100 °C. at 0.01s^{-1}. At 927 °C, the Top region shows the strongest texture (17.80mrd), indicating pronounced orientation preferences likely due to limited dynamic recrystallization (DRX). The Center (10.03mrd) and Bottom (9.88mrd) regions display moderately weaker textures, suggesting more active DRX processes. When the temperature increases to 1000 °C, the texture strength distribution changes significantly: the Top region weakens (11.01 mrd) while the Center shows the weakest texture (4.34 mrd), indicating extensive DRX. Interestingly, the Bottom region develops the strongest texture at this temperature (14.98 mrd), potentially due to preferential grain growth or strain localization effects. These results demonstrate that texture evolution is highly sensitive to both temperature and spatial position. The Bottom region exhibits an unexpected texture strengthening at higher temperatures, warranting further investigation into the underlying deformation mechanisms. The inverse relationship between texture strength in the center and bottom regions with increasing temperature suggests complex, competing processes of DRX and orientation development during thermo-mechanical processing.

At a constant strain rate of 0.01 s^{-1}, both grain size and texture intensity show clear temperature-dependent trends. At 927 °C, limited DRX leads to large grains in the top and bottom regions and a high texture intensity across the specimen, reflecting strong retention of deformation-induced orientations. At 1000 °C, increased DRX produces finer grains, especially in the center, and a corresponding reduction in texture intensity, with the center retaining the strongest texture due to partially recrystallized but still deformation-influenced grains. At 1100 °C, extensive DRX followed by grain coarsening results in moderate grain growth in the center and significant coarsening at the top and bottom. Texture becomes weakest in the center due to strong orientation

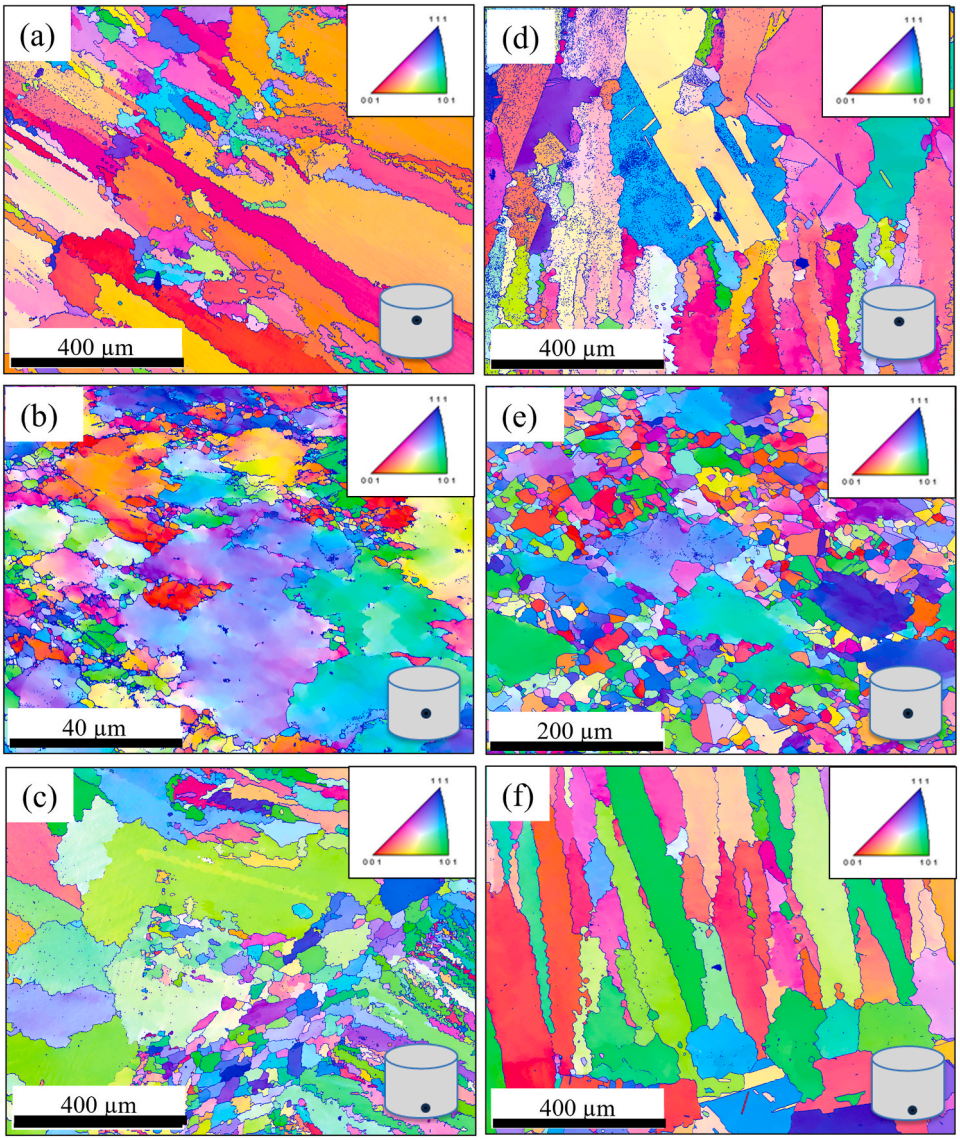

Fig. 14. EBSD maps of the HCT sample deformed at a strain rate 0.01 s^{-1}, showing the Top, Center, and Bottom regions: (a–c) at 927 °C and (d–f) at 1100 °C.

randomization, while the top and bottom show stronger textures linked to preferential growth of oriented grains. Overall, higher temperatures promote DRX and reduce texture intensity, with the most pronounced effects occurring in the center region.

It is important to identify the critical processing conditions at which dynamic recrystallization (DRX) becomes the primary softening mechanism. To achieve this, a polynomial model is proposed for determining this region.

The variation in recrystallized grain size can be described as a function of the Zener–Hollomon parameter using the following second-order polynomial equation:

$$DDR_X = 0.0233(ln(Z))^2 - 2.9012(ln(Z)) + 89.284 \quad (7)$$

The proposed model above can be used to predict the recrystallized grain size during the hot deformation of WAAM-processed IN718. Application of Zener Hollomon involves some assumptions and inherent limitations. Z assumes a constant activation energy (Q) and a single dominant thermally activated deformation mechanism, although in practice, Q can vary with strain, temperature, and evolving microstructure, and mechanisms such as dynamic recovery and dynamic recrystallization may simultaneously occur. The model also presumes isothermal and homogeneous deformation, while hot compression tests often exhibit frictional heating, strain gradients, and localized flow. Additionally, Z is highly sensitive to the selected activation energy and does not explicitly account for microstructural evolution such as recrystallized fraction, grain refinement, or dislocation density changes. Therefore, while Z provides a useful framework for comparing processing conditions, its predictions should be interpreted in the context of these assumptions and limitations.

The experimental and predicted recrystallized grain sizes for the WAAM-processed and wrought IN718 are shown in Fig. 17 [55]. The predicted grain sizes were then compared with the experimental values, and an error of approximately 4.8 % was observed. It is evident that higher Z values promote the formation of finer recrystallized grains in both as-printed IN718 and wrought material, particularly following hot deformation at 927 °C and 1000 °C under strain rates of $1s^{-1}$ and $5s^{-1}$. This trend is consistent with the findings of Mostafa [23] for SLM-processed IN718 superalloys, Lan et al. [33] for WAAM IN718 superalloys, and Ozturk et al. [56] for wrought IN718. This may be ascribed to the tendency of recrystallized grains to coarsen more readily at lower strain rates and higher temperatures within the forming temperature range. It is noteworthy that dynamic recrystallization appears to be the predominant softening mechanism in deformation regimes where $ln(Z) \geq 44.5$. From an additive manufacturing preform and

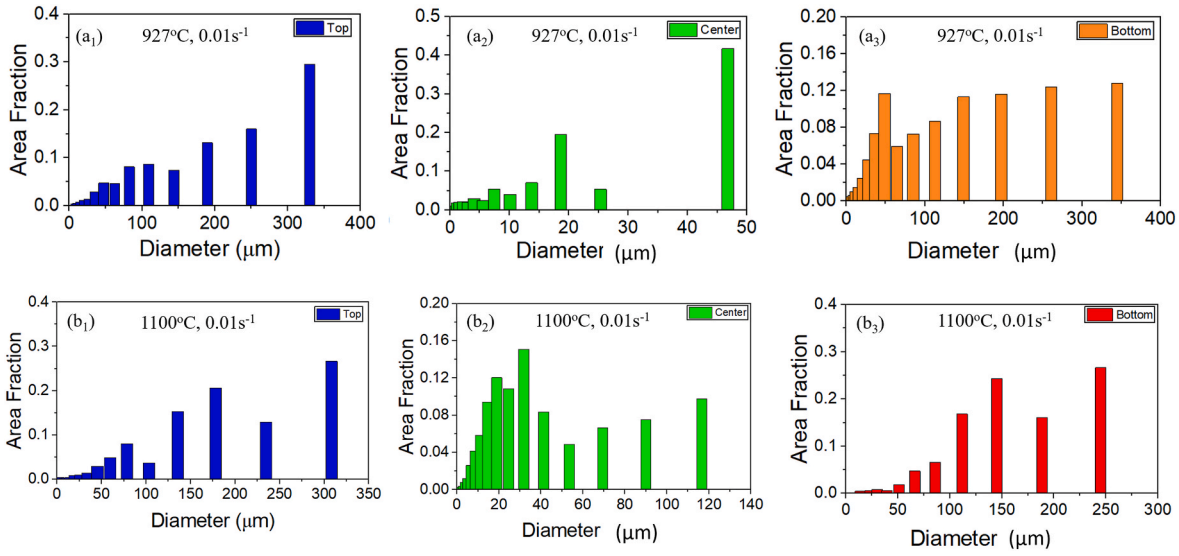

Fig. 15. EBSD grain size distribution of the HCT sample deformed at strain rate 0.01 s-1, showing the Top, Center, and Bottom regions: (a_1-a_3) at 927°C and (b_1-b_3) at 1100°C.

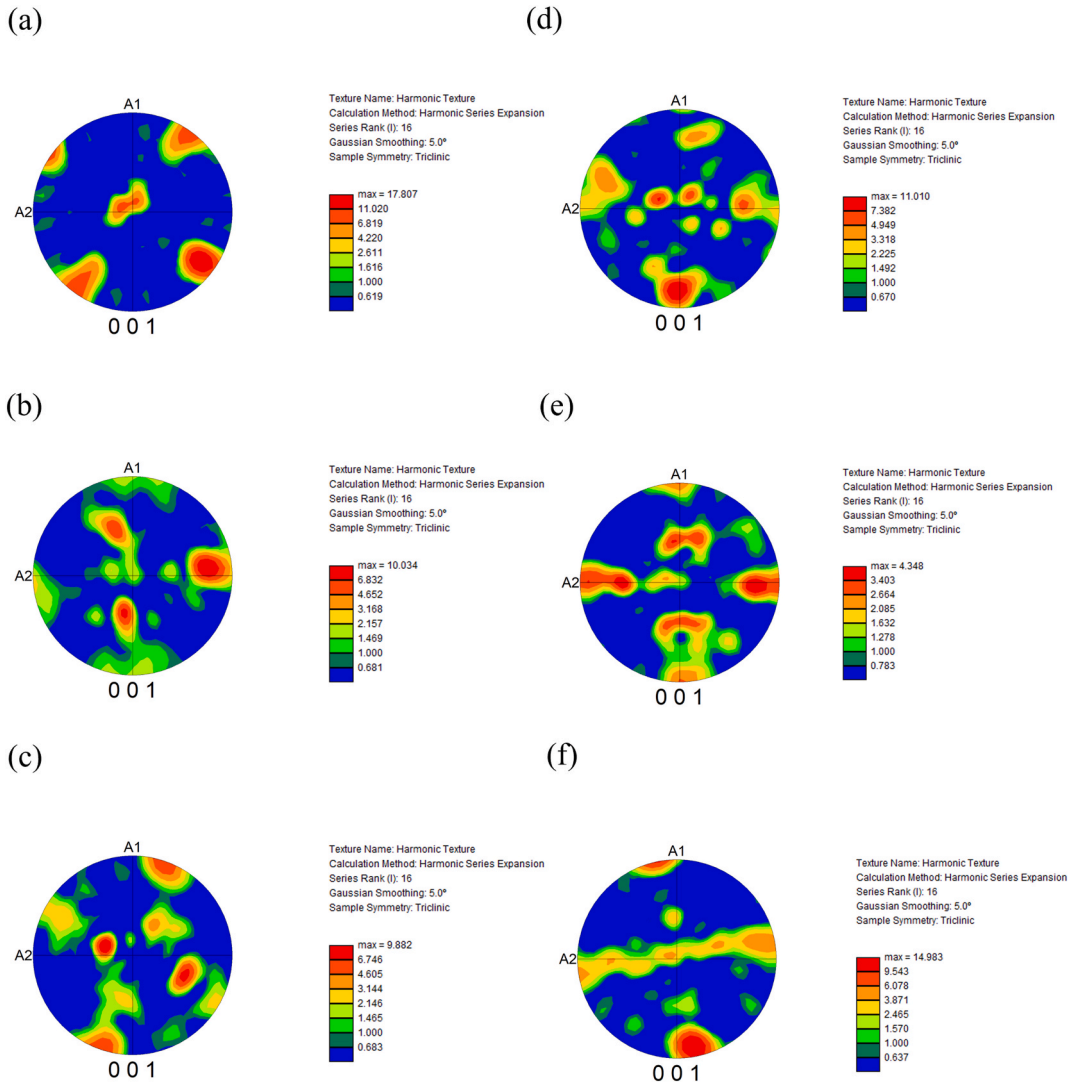

Fig. 16. Pole figures of the sample compressed at a strain rate of $0.01s^{-1}$, showing the Top (a, d), Center (b, e), and Bottom (c, f) regions at 927 °C (a–c) and 1100 °C (d–f).

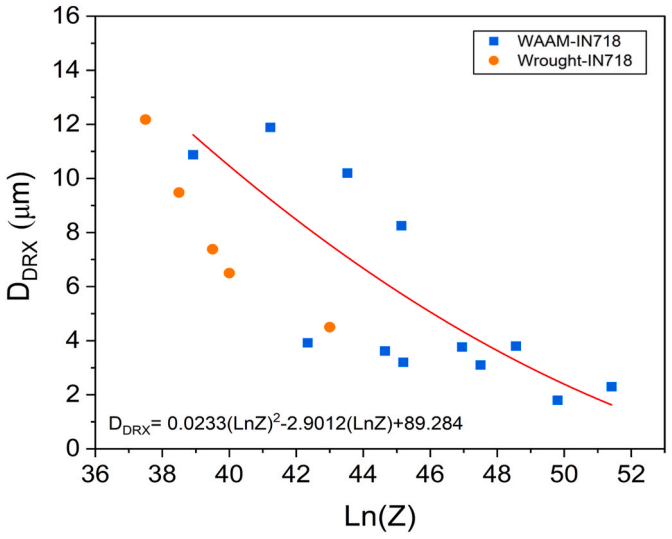

Fig. 17. Plot represents the variation of recrystallized grain size with Zener Hollomon parameter.

forging perspective, the model confirms that WAAM-processed IN718 achieves finer recrystallized grains and thus better microstructural refinement when forged in high-Z regimes (high strain rate, lower temperature), where DRX dominates. Conversely, forging at low-Z conditions promotes grain coarsening, underscoring the need to control strain rate and temperature to optimize post-AM mechanical properties.

3.4. EDS elemental analysis

Area elemental mapping was performed on WAAM samples subjected to HCT, and the results are presented in Figs. 18 and 19. Fig. 18 depicts elemental mapping of the primary alloy constituents (Fe, Nb, Mo, Cr, Ni) in addition to Ti and C. Across all HCT conditions, this data indicates a typical IN718 matrix rich in Ni, Cr, and Fe. Localized regions with higher concentrations of Nb, Mo, and Ti are present at the micron length scale, with possible local depletion of Ni, Fe, and Cr in the same regions. However, there was no evidence of TiC precipitates. The precipitate pattern for samples at 927 °C and 1000 °C is similar to that of as-printed additively manufactured IN718 material. This suggests that HCT at these temperatures may not be sufficiently energetic to alter the precipitate patterns established during additive manufacturing, which are dominated by melt-pool dynamics and solidification processes. However, the sample processed at the highest temperature (1100 °C, 0.01 s^{-1}) shows a distinct pattern, where the precipitates are less evident and have a more dispersed, equiaxed morphology. This suggests that a temperature of 1100 °C provides sufficient diffusion to alter the precipitate pattern strongly.

Fig. 19 shows the overall elemental composition, and Table 4 shows the elemental analysis for all 4 HCT processing conditions. Overall, all samples showed a composition consistent with that of base IN718, within the detection limits and accuracy typical for quantitative energy dispersive X-ray spectroscopy.

As stated in the initial microstructure evolution of the WAAM-processed Inconel 718 preform, Laves phases originate from micro-segregation during solidification. This process is significantly reduced by applying a homogenization treatment, typically involving annealing above [33]. These detrimental phases can be 1100 °C for approximately 1 h prior to hot deformation. The presence of Laves phases is known to deteriorate tensile strength and fatigue performance [57]. However, the present study aimed to develop a hybrid additive-forging approach by integrating AM with hot forging. Therefore, homogenization treatment of the AM-processed samples was not considered within the scope of this work.

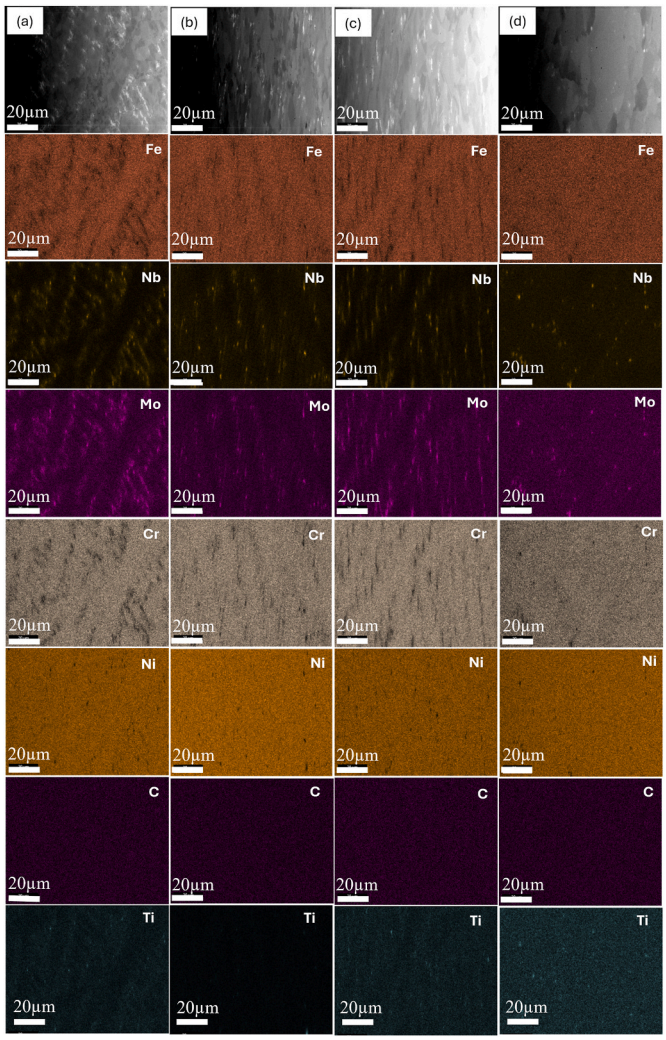

Fig. 18. Microstructure and elemental composition maps (EDS) of hot-compressed WAAM samples at: (a) 927 °C, 0.01 s^{-1}, (b) 1000 °C, 0.01 s^{-1}, (c) 1000 °C, 5 s^{-1}, and (d) 1100 °C, 0.01 s^{-1}.

3.5. Optimization of the hot workability window for WAAM-processed - Inconel 718

Processing maps for IN718 were developed based on the Dynamic Materials Model (DMM) proposed by Prasad et al. [58], which treats the sample as a dissipater of power during hot deformation. The total power input P at a specific temperature and strain rate can be written as follows:

$$P = \sigma\dot{\varepsilon} = G + J \tag{8}$$

Where G denotes the power dissipated through plastic deformation and J denotes the energy dissipated through microstructural changes such as dynamic recovery and dynamic recrystallization. The strain rate sensitivity m at a constant strain and temperature is determined from the slope of natural log of true stress ($ln\ \sigma$) vs natural log of strain rate ($ln\ \dot{\varepsilon}$) by using the dynamic response of the material:

$$\sigma = K\dot{\varepsilon}^m \tag{9}$$

Where K is a material constant and m is strain rate sensitivity, given by

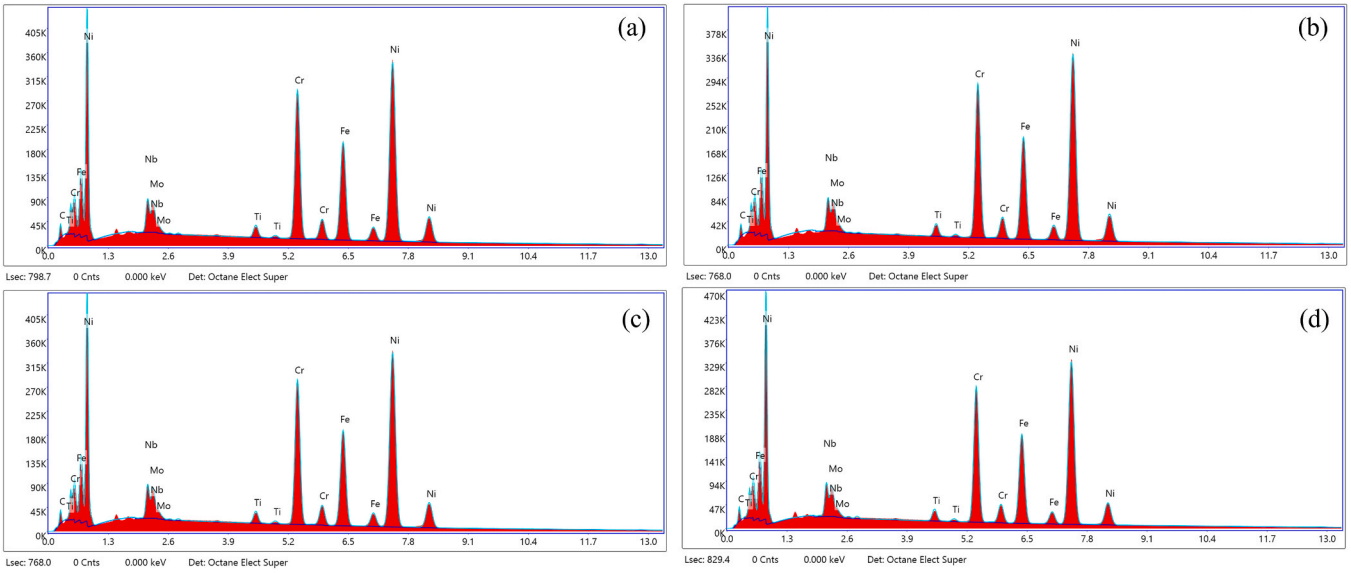

Fig. 19. EDS Spectrum of hot-compressed WAAM samples at: (a) 927 °C, 0.01 s^{-1}, (b) 1000 °C, 0.01 s^{-1}, (c) 1000 °C, 5 s^{-1}, and (d) 1100 °C, 0.01 s^{-1}.

Table 4
EDS elemental analysis results % weight of detected elements-numbers corresponds to those in Fig. 19.

Temperature (°C)	Strain Rate (s^{-1})	Nb	Mo	Ti	Cr	Fe	Ni	C
927	0.01	4.03	2.25	1.17	20.06	18.41	51.49	2.60
1000	0.01	3.86	2.14	1.17	20.60	18.59	51.86	2.25
1000	5	4.16	2.27	1.18	20.25	17.35	51.38	2.60
1100	0.01	4.39	2.44	1.24	19.89	18.23	50.84	2.96

$$m = \frac{d(ln\,\sigma)}{d(ln\dot{\varepsilon})} \tag{10}$$

Using equations (8) and (9), J can be derived as

$$J = \left(\frac{m}{m+1}\right)\sigma\dot{\varepsilon} \tag{11}$$

The highest attainable power dissipation through microstructural changes is achieved when the strain-rate sensitivity m equals 1 [32]. In hot deformation, the efficiency η is defined as the ratio between the experimentally measured power dissipated through microstructural changes and its maximum possible value. Accordingly, the strain rate sensitivity m of the flow stress becomes a key parameter governing the efficiency of thermomechanical processing.

$$\eta = \frac{J}{J_{max}} = \frac{2m}{m+1} \tag{12}$$

This parameter reflects the relative contribution of microstructural processes to the total power dissipation. Contour maps of η were generated over a domain of deformation temperature (927–1100 °C) and strain rate (0.01–5 s^{-1}) at a constant true strain of 0.4. Flow instability during hot deformation was evaluated using the instability parameter ξ proposed by Prasad et al. [58].

$$\xi = \frac{\partial ln\left(\frac{m}{m+1}\right)}{\partial ln\dot{\varepsilon}} + m > 0 \tag{13}$$

Negative values of ξ indicate flow instability, such as adiabatic shear localization, flow localization, or cracking. These instability regions were superimposed on the power dissipation efficiency maps shown in Fig. 20 to obtain the final processing maps. Regions of high η coupled with ξ > 0 were identified as the optimal processing domains for hot deformation of IN718.

The processing map analysis shown in Fig. 20 revealed that the most

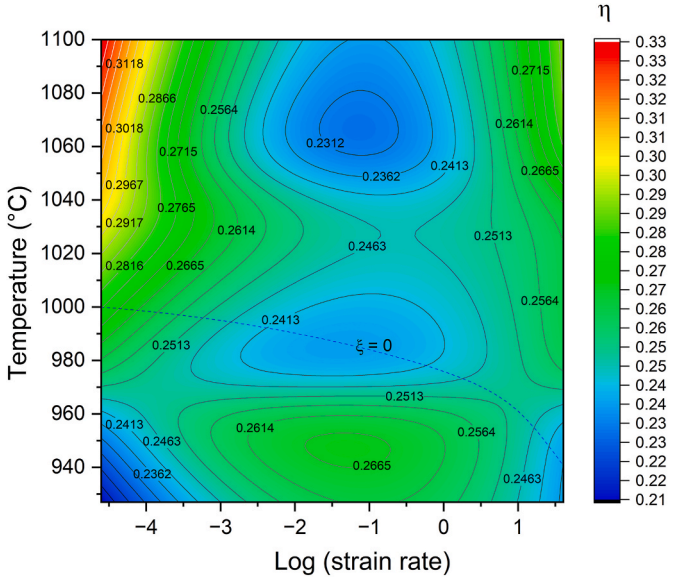

Fig. 20. Processing map for Inconel 718 in the temperature range 927°C–1100°C and strain rate 0.01s^{-1} to 5s^{-1} based on dynamic materials model.

favorable hot-working window for IN718 lies at 1100 °C and strain rates of 1–5 s^{-1}, where higher strain-rate sensitivity and efficiency of power dissipation indicate dynamic recrystallization as the dominant mechanism, ensuring stable deformation at relatively low flow stresses. A secondary workable domain was identified around 1000 °C at 1 s^{-1}, which also exhibited reasonable efficiency and stability. In contrast, deformation at 927 °C and higher strain rates (5 s^{-1}) showed negative

instability parameters, suggesting a tendency toward localized flow and cracking, and should therefore be avoided.

4. Conclusions

This study investigated and discussed the mechanical response of heat-treated, additively manufactured Inconel 718 alloy at various temperatures and strain rates, focusing on flow stress, crystallographic texture, grain size, and microstructural characteristics.

- As-deposited WAAM microstructure consisted of coarse columnar grains (438 μm) with dendritic/interdendritic segregation and Nb/Ti-rich Laves phases along dendrite arms, influencing subsequent deformation behavior.
- The activation energy for hot deformation was calculated as 472.05 kJ/mol higher than typical wrought IN718 due to solidification-driven heterogeneities and residual stresses, which increase resistance to dynamic softening.
- Flow behavior was strongly governed by deformation conditions: higher temperatures and lower strain rates promoted DRV/DRX and reduced flow stress, whereas low temperatures and high strain rates inhibited softening, resulting in higher peak stresses.
- Restoration mechanisms varied with strain rate: DRX dominated at 5 s^{-1}, while DRV prevailed at 0.01 s^{-1}. Peak stresses ranged from 589 MPa (927 °C, 5 s^{-1}) to 88 MPa (1100 °C, 0.01 s^{-1}).
- EBSD results showed non-uniform DRX grain refinement, with the center region experiencing the most significant grain breakup. These findings confirm that a true strain of ~0.4 is sufficient to eliminate columnar grains, enabling near-net-shape AM preform designs with reduced waste and tooling requirements.
- A Zener–Hollomon parameter-based model effectively predicted recrystallized grain size, with fine grains forming under high-Z (high strain rate/low temperature) conditions.
- Processing maps indicated the optimal hot-working window for WAAM IN718 as 1100 °C at 1-5 s^{-1}, with a secondary stable domain at 1000 °C and 1 s^{-1}. Instability was observed at 927 °C, particularly at higher strain rates.

Overall, the results provide practical guidance for transitioning to AM-enabled forging workflows, demonstrating that WAAM-produced preforms can be reliably integrated into industrial forging routes. In future work, WAAM-fabricated preforms for aircraft components will be forged with industry partners to validate preform design strategies and further mature hybrid AM-forging processing routes.

Disclaimer

The views and conclusions contained herein are those of the authors and should not be interpreted as necessarily representing the official policies or endorsements, either expressed or implied, of Air Force Research Laboratory or the U.S. Government.

Declaration of competing interest

The authors declare the following financial interests/personal relationships which may be considered as potential competing interests: Tushar Borkar reports financial support was provided by Cleveland State University. If there are other authors, they declare that they have no known competing financial interests or personal relationships that could have appeared to influence the work reported in this paper.

Acknowledgment

This material is based on research sponsored by Air Force Research Laboratory under agreement number FA8650-20-2-5700. The U.S. Government is authorized to reproduce and distribute reprints for Governmental purposes, notwithstanding any copyright notation thereon.

References

[1] Bambach, M. and I. Sizova. Hot working behavior of selective laser melted and laser metal deposited inconel 718. AIP Publishing.
[2] Habibiyan A, Hanzaki AZ, Abedi HR. An investigation into microstructure and high-temperature mechanical properties of selective laser-melted 316L stainless steel toward the development of hybrid ampliforge process. Int J Adv Manuf Technol 2020;110:383–94.
[3] International, A.. Astm F3187-16: standard guide for directed energy deposition of metals. 2016.
[4] Williams, S.W., et al., Wire þ arc additive manufacturing.
[5] Seow CE, et al. Wire+ arc Additively Manufactured Inconel 718: effect of post-deposition heat treatments on microstructure and tensile properties. Mater Des 2019;183:108157.
[6] Va S, Na B. A study on microstructure and mechanical properties of inconel 718 superalloy fabricated by novel CMT-WAAM process. Mater Res 2024;27:e20230258.
[7] James WS, Ganguly S, Pardal G. High temperature performance of wire-arc additive manufactured inconel 718. Sci Rep 2023;13(1):4541.
[8] Li N, Wang C, Li C. Microstructures and high-temperature mechanical properties of inconel 718 superalloy fabricated via laser powder bed fusion. Materials 2024;17(15):3735.
[9] Schneider J, et al. Microstructure evolution in inconel 718 produced by powder bed fusion additive manufacturing. J Manuf Mater Process 2022;6(1):20.
[10] Dinh DM, Pham QH. Wire and arc additive manufacturing of inconel alloys: a review on microstructures, mechanical properties, and common defects. 2024.
[11] Ravichander BB, et al. A prediction model for additive manufacturing of inconel 718 superalloy. Applied Sciences 2021;11(17):8010.
[12] Song J, et al. Unusually high room and elevated-temperature tensile properties observed in direct aged wire-arc directed energy deposited inconel 718. Sci Rep 2023;13(1):19235.
[13] Huang L, et al. A review of challenges for wire and arc additive manufacturing (WAAM). Trans Indian Inst Met 2023;76(5):1123–39.
[14] Panov D, et al. The effect of post-deposition heat treatment on the microstructure, texture, and mechanical properties of inconel 718 produced by hybrid wire-arc additive manufacturing with inter-pass forging. Metals 2025;15(1):78.
[15] Alcoa corporation. [cited 2025 06/23/2025]; Available from:: https://news.alcoa.com/press-releases/press-release-details/2015/Alcoa-Expands-RD-Center-to-Deepen-Additive-Manufacturing-Capabilities/default.aspx.
[16] Meiners F, et al. New hybrid manufacturing routes combining forging and additive manufacturing to efficiently produce high performance components from Ti-6Al-4V. Procedia Manuf 2020;47:261–7.
[17] Kamal M, Rizza G. Design for metal additive manufacturing for aerospace applications. In: Additive manufacturing for the aerospace industry. Elsevier; 2019. p. 67–86.
[18] Tao P, et al. Microstructure, mechanical properties, and constitutive models for Ti–6Al–4V alloy fabricated by selective laser melting (SLM). Metals 2019;9(4):447.
[19] Qiu C, Adkins NJE, Attallah MM. Microstructure and tensile properties of selectively laser-melted and of HIPed laser-melted Ti–6Al–4V. Materials Science and Engineering: A 2013;578:230–9.
[20] Blackwell PL. The mechanical and microstructural characteristics of laser-deposited IN718. J Mater Process Technol 2005;170(1–2):240–6.
[21] Wycisk E, et al. Fatigue performance of laser additive manufactured Ti–6Al–4V in very high cycle fatigue regime up to 109 cycles. Front Mater 2015;2:72.
[22] Roush ED, Kobryn PA, Semiatin SL. Anisotropy of plastic flow and microstructure evolution during hot working of laser-deposited Ti–6Al–4V. Scr Mater 2001;45(6):717–24.
[23] Mostafa A, et al. Hot compression behavior and microstructure of selectively laser-melted IN718 alloy. Int J Adv Manuf Technol 2018;96:371–85.
[24] Abedi HR, et al. The high temperature flow behavior of additively manufactured inconel 625 superalloy. Mater Res Express 2019;6(11):116514.
[25] Sizova I, Bambach M. Hot workability and microstructure evolution of pre-forms for forgings produced by additive manufacturing. J Mater Process Technol 2018;256:154–9.
[26] Kusekar Sambhaji, et al. Laser Powder Bed Fusion and Hot Forging of 316L Stainless Steel: A Hybrid Additive Manufacturing Approach for Enhanced Performance. Materials 2025;18.21:4909.
[27] Lin H, et al. Ultrasonic rolling-enhanced additive manufacturing of IN718 superalloy: microstructural refinement and mechanical property improvement through variable power modulation. Addit Manuf 2025:104891.
[28] Tan C, et al. Review on field assisted metal additive manufacturing. Int J Mach Tool Manufact 2023;189:104032.
[29] Chen Q, et al. Research on microstructure and mechanical properties of hybrid plasma arc and micro-rolling additive manufacturing of Inconel 718 superalloy. Rapid Prototyp J 2022;28(8):1509–19.
[30] Du Y, et al. A review of deep learning in metal additive manufacturing: impact on process, structure, and properties. Prog Mater Sci 2025:101587.
[31] Na Y-S, et al. Prediction of microstructure evolution during high temperature blade forging of a Ni− Fe based superalloy, alloy 718. Met Mater Int 2003;9(1):15–9.
[32] Gupta C, et al. Correlating hot deformation parameters with microstructure evolution during thermomechanical processing of inconel 718 alloy. Metall Mater Trans 2019;50(10):4714–31.

[33] Lan B, et al. The influence of microstructural anisotropy on the hot deformation of wire arc additive manufactured (WAAM) inconel 718. Materials Science and Engineering: A 2021;823:141733.
[34] Sujan GK, et al. Hot deformation behavior and microstructural evolution of wire-arc additively fabricated inconel 718 superalloy. Metall Mater Trans 2023;54(1):226–40.
[35] Dhondapure P, et al. Influence of deformation path on the stress state and damage evolution along the central axis of a large size forged ingot of AISI H13 steel. J Mater Res Technol 2023;27:8244–57.
[36] Hawker C, Reed J. Metallurgical impact of switching from hammer units to hydraulic presses for forging. 2024.
[37] Bhaduri A. Mechanical properties and working of metals and alloys, vol. 264. Springer; 2018.
[38] Yangfan W, Xizhang C, Chuanchu S. Microstructure and mechanical properties of inconel 625 fabricated by wire-arc additive manufacturing. Surf Coating Technol 2019;374:116–23.
[39] Wang Y, Chen X. Investigation on the microstructure and corrosion properties of inconel 625 alloy fabricated by wire arc additive manufacturing. Mater Res Express 2019;6(10):106568.
[40] Liu F, et al. Laves phase control of inconel 718 superalloy fabricated by laser direct energy deposition via δ aging and solution treatment. J Mater Res Technol 2020;9(5):9753–65.
[41] Kindermann RM, et al. Process response of inconel 718 to wire+ arc additive manufacturing with cold metal transfer. Mater Des 2020;195:109031.
[42] Kunze K, et al. Texture, anisotropy in microstructure and mechanical properties of IN738LC alloy processed by selective laser melting (SLM). Materials Science and Engineering: A 2015;620:213–22.
[43] Ma D, et al. Crystallographic texture in an additively manufactured nickel-base superalloy. Materials Science and Engineering: A 2017;684:47–53.
[44] Xi N, et al. Wire arc additive manufacturing of inconel 718: constitutive modelling and its microstructure basis. J Manuf Process 2022;75:1134–43.
[45] Gudur S, et al. A study on the effect of substrate heating and cooling on bead geometry in wire arc additive manufacturing and its correlation with cooling rate. Mater Today Proc 2021;41:431–6.
[46] Dong B, et al. Effects of interlayer temperature on the microstructures of wire arc additive manufactured al-zn-mg-cu alloy: insights into texture responses and dynamic precipitation behaviors. Addit Manuf 2021;48:102453.
[47] Yoo J, et al. Investigation of hydrogen embrittlement properties of Ni-based alloy 718 fabricated via laser powder bed fusion. Int J Hydrogen Energy 2022;47(43):18892–910.
[48] Chamanfar A, et al. Evolution of flow stress and microstructure during isothermal compression of waspaloy. Materials Science and Engineering: A 2014;615:497–510.
[49] Guimaraes AA, Jonas JJ. Recrystallization and aging effects associated with the high temperature deformation of waspaloy and inconel 718. Metall Trans A 1981;12:1655–66.
[50] Chamanfar A, et al. Analysis of flow stress and microstructure during hot compression of 6099 aluminum alloy (AA6099). Materials Science and Engineering: A 2019;743:684–96.
[51] Ji G, et al. A comparative study on Arrhenius-type constitutive model and artificial neural network model to predict high-temperature deformation behaviour in Aermet100 steel. Materials Science and Engineering: A 2011;528(13–14):4774–82.
[52] Dhondapure P, et al. Influence of deformation path on microstructure evolution during the open die forging of large size ingot of high strength steel: experiments and FE analysis. Int J Adv Manuf Technol 2024;134(7):3733–50.
[53] Yuan H, Liu WC. Effect of the δ phase on the hot deformation behavior of inconel 718. Materials Science and Engineering: A 2005;408(1–2):281–9.
[54] Nowotnik A, et al. Mechanical properties of hot deformed inconel 718 and X750. Journal of Achievements in Materials and Manufacturing Engineering 2012;50(2):74–80.
[55] Wang Y, et al. Flow behavior and microstructures of superalloy 718 during high temperature deformation. Materials Science and Engineering: A 2008;497(1–2):479–86.
[56] Ozturk U, Maria Cabrera J, Calvo J. High-temperature deformation of inconel 718plustm. J Eng Gas Turbines Power 2017;139(3):032101.
[57] Chen H, et al. Experimental investigation of the Nb-Ni phase diagram. J Mater Sci 2005;40(22):6019–22.
[58] Prasad Y, et al. Modeling of dynamic material behavior in hot deformation: forging of Ti-6242. Metall Trans A 1984;15(10):1883–92.